Applied Thermal Engineering 278 (2025) 126964

Contents lists available at ScienceDirect

Applied Thermal Engineering

journal homepage: www.elsevier.com/locate/ate

Research Paper

Multiphysics modeling of open-water evaporation: Quantifying the natural convection effects of water

Peixin Dong [a,1], Haoran Chang [a,1], Nan Deng [a], Su Guo [b,c], Mengying Li [a,*]

[a] Department of Mechanical Engineering & Research Institute for Smart Energy, The Hong Kong Polytechnic University, Hong Kong Special Administrative Region
[b] School of Renewable Energy, Hohai University, Nanjing, China
[c] Nanjing Jurun Information Technology Co., Ltd, Nanjing, China

ARTICLE INFO

Keywords:
Open-water evaporation
3-D multiphysics model
Natural convection
Relative humidity
Air–water interface temperature
Roll pattern

ABSTRACT

In this study, we develop a three-dimensional (3-D) numerical model using COMSOL Multiphysics to estimate water evaporation from open-water bodies, rigorously validated against experimental data from the literature, demonstrating satisfactory accuracy. Through comprehensive simulations, we elucidate the evolving patterns of evaporation with natural convection in diverse environmental conditions, including temperature, wind speed, and relative humidity. Specifically, under windless conditions, the evaporation rate initially decreases due to moisture accumulation and subsequently increases, as determined by the temperature at the air–water interface. In contrast, under windy conditions, the evaporation rate consistently decreases, solely dictated by this temperature. In addition, our findings underscore the critical role of natural convection within the water body in influencing evaporation rates under both windy and windless conditions. Specifically: 1) Neglecting the contribution of natural convection within the water body results in significant discrepancies in evaporation rate estimations, over 2.5 times in windless conditions, 2.5 times at 2 m/s, and 1.5 times at 5 m/s, due to the lower heat transfer rate of conduction compared to convection. 2) In the absence of external heat input, the omission of natural convection reduces the evaporation rate by 2 times under windless conditions, 1.05 times at 2 m/s, and 1.02 times at 5 m/s. Finally, the roll pattern of Rayleigh–Bénard convection in a water body is analyzed, which is primarily dominant by external heat, even in windy conditions. Without external heat, the wind takes over as the main factor affecting the evaporation rate. In the absence of both external heat and wind, natural convection in the air becomes the dominant factor for evaporation. This numerical investigation expands the validity of current methods for estimating evaporation from open-water bodies under complex environmental conditions.

1. Introduction

Accurate estimation of open water evaporation rates from lakes, ponds and reservoirs is paramount in various disciplines, including water resource management, climate science, ecosystem sustainability, and architectural design [1,2]. For instance, in the realm of building design, a comprehensive understanding of the evaporation rates from adjacent open-water bodies is crucial for urban planners and architects. These rates significantly influence the local microclimate, energy consumption patterns, and cooling strategies used in urban environments. Elevated evaporation rates can alter humidity levels in the vicinity of buildings, thus affecting thermal comfort and necessitating effective water management strategies for features such as ponds, pools, and fountains [3,4]. Recent investigations [5,6] underscore the implications of evaporation on urban heat islands and overall building performance, based on the foundational work of Penman [7], which established essential principles for understanding evaporation processes.

The evaporation process is governed by intricate heat and mass transfer mechanisms occurring at the air–water interface, influenced by a multitude of factors on both the air and water sides. Key determinants include air and water temperatures, vapor pressure, relative humidity, turbulent mixing induced by wind, and the physical dimensions of the water body [8,9]. The relationship between evaporation rates and these influencing variables has been the subject of extensive investigation through a variety of experimental studies [10,11], alongside a limited number of theoretical formulations and even fewer numerical models [12].

Experimental investigations can be broadly classified into indoor and outdoor tests. Indoor experiments, commonly referred to as free

* Corresponding author.
E-mail address: mengying.li@polyu.edu.hk (M. Li).
[1] These two authors contributed equally to this work.

https://doi.org/10.1016/j.applthermaleng.2025.126964
Received 13 September 2024; Received in revised form 12 May 2025; Accepted 26 May 2025
Available online 9 June 2025

evaporation tests, are conducted in controlled laboratory environments without wind, focusing primarily on heat and mass transfer phenomena driven by molecular diffusion. These controlled conditions facilitate the precise regulation of the experimental parameters, employing similarity laws to simulate real-world scenarios [13,14]. For example, Misyura et al. [15] explored the evaporative behavior of a water layer and the corresponding heat transfer dynamics under localized laser heating, unveiling innovative methodologies for enhancing heat exchange. In contrast, outdoor experiments, known as forced evaporation tests, encompass the combined effects of advection, where wind-driven air movement interacts with the air–water interface, and diffusion [11,16]. These studies frequently use evaporation pans situated in environments such as reservoirs, lakes, and outdoor pools [17,18]. Although pan evaporation represents a straightforward and cost-effective measurement approach [19,20], it introduces uncertainties due to reliance on databases from sites that may not accurately reflect the specific water body under investigation, such as Class A pans at meteorological stations [21].

Furthermore, critical factors such as depth of water, surface area, material composition, structural characteristics, positioning, and salinity levels can significantly influence evaporation rates [22–24]. Although higher-accuracy techniques, such as eddy covariance, offer more accurate measurements, they often involve substantial costs and resource demands. Consequently, long-term studies focused on small open-water reservoirs remain relatively scarce, limiting a comprehensive understanding of evaporation dynamics within these environments [25].

Empirical correlations derived from field experiments are frequently employed to quantify the relationship between evaporation rates and their influencing factors. These correlations can be broadly categorized into two main types: those based on Dalton's law [26] and those based on the analogy between heat and mass transfer [27]. Correlations based on Dalton's law conceptualize water evaporation as being proportional to the differential vapor pressure between the open-water surface and the moisture content in the overlying air. This relationship is typically articulated as $E = (A + BV)(p_{v,s} - \Phi p_{v,\infty})/h_{fg}$, where E represents the evaporation rate, A and B are empirical constants, Φ denotes relative humidity, h_{fg} is the latent heat of vaporization of water, and V is the wind speed. The second category of correlations, often referred to as similarity theory, posits that convective heat and mass transfer processes are analogous. This theory applies the principles of convective heat transfer to estimate mass transfer rates by substituting traditional parameters such as the Prandtl number and the Reynolds or Grashof number with the Schmidt number and the mass transfer Reynolds or Grashof number, respectively. Recently, Muneeshwaran et al. [28] introduced a universal correlation for falling film evaporation that is applicable to both freshwater and seawater, demonstrating improved predictive accuracy across a diverse array of datasets. Despite their widespread application, these empirical correlations exhibit certain limitations. For instance, significant variability in the coefficients A and B in Dalton's law can occur due to measurements taken at inconsistent heights. Additionally, these correlations are generally constrained to specific conditions, such as a limited range of air and water temperatures, relative humidity, and wind speed [29]. Although efforts have been made to broaden the applicability of these correlations with reasonable accuracy [11], deviations are frequently observed when conditions fall outside the specified ranges.

Given the inherent limitations of empirical correlations and experimental tests, numerical methods have emerged as a compelling alternative for quantifying water evaporation, particularly with the help of computational fluid dynamics (CFD) tools such as COMSOL Multiphysics, ANSYS Fluent, and Star-CCM+ [30]. For example, Raimundo et al. [10] elucidated the intricate relationship between evaporation from a heated water surface and the thermal properties of the surrounding environment through a 3-D CFD simulation. These numerical methods have demonstrated a robust ability to accurately estimate water evaporation under various environmental conditions, presenting distinct advantages over traditional experimental approaches. A notable application of numerical analysis in this field involves improving thermal comfort in swimming pools, where Blázquez et al. [31] employed ANSYS Fluent to develop a numerical model that estimated evaporation rates in indoor swimming pools, achieving a relative error of merely 3% compared to full-scale experimental results. This CFD-based methodology was further refined by Gallero et al. [32] to minimize estimation errors under forced convection conditions. In addition, several studies have identified critical factors that influence water evaporation through numerical simulations [33,34], with Luo et al. [2] exploring thermal design strategies to improve interfacial evaporation. However, it is important to note that previous studies have often treated swimming pools as surfaces with uniform temperatures, overlooking internal natural convection within the water body. This simplification can lead to an overestimation of evaporation rates, especially in smaller open-water bodies, where internal convection significantly influences heat and mass transfer processes. The importance of internal convection has been underscored by Bower and Saylor [13], yet its quantitative investigation remains largely unaddressed. To address this gap, a multiphysics CFD model has been developed to examine the effects of internal circulation within open-water bodies on evaporation rates.

In summary, while existing studies can numerically simulate the evaporation process for open-water bodies under various environmental conditions, several critical physical processes are often simplified based on assumptions. In particular, the internal flow induced by natural convection in open-water bodies is often ignored, which means that the evaporation process is not directly connected to the internal flow. However, ignoring the internal circulation could lead to significant discrepancies in the estimations of the evaporation rate. In this work, we present a transient 3-D multiphysics model that couples forced convection by wind, water evaporation, vapor diffusion, and natural convection within the water body using COMSOL Multiphysics as presented in Section 2. The critical importance of incorporating natural convection within the water body is presented in Section 3, where a comparative analysis quantitatively assesses its significance. Following this, Section 4 summarizes the primary contributions of this study, and an Appendix is provided, containing robust validations for the numerical model.

2. Numerical model for the open-water body evaporation

The transient evaporation process of an open-water body, driven by external heat sources such as solar radiation, involves the interplay of multiple physics. Technically, four key aspects must be considered simultaneously to simulate the evaporation process of an open-water body, as illustrated in Fig. 1:

(I) the turbulent airflow above the open-water body.

(II) the transport of mass and energy from water to air via evaporation.

(III) the natural convection within the open-water body.

(IV) the absorption of radiation as heat.

2.1. Problem description

In this study, the commercial software COMSOL Multiphysics [35] is used to simulate the evaporation of an open-water body. A 3-D numerical model is established that comprises an open-water body and a free air zone with the specific dimensions depicted in Fig. 2. The open-water body is represented as a cuboid, characterized by a depth of 0.3 m and a square cross-section with equal width and length of 1 m. Furthermore, a free air zone is configured with dimensions of 4 m × 2 m × 1 m (length × width × height), respectively. The numerical model is then developed on the basis of several key assumptions.

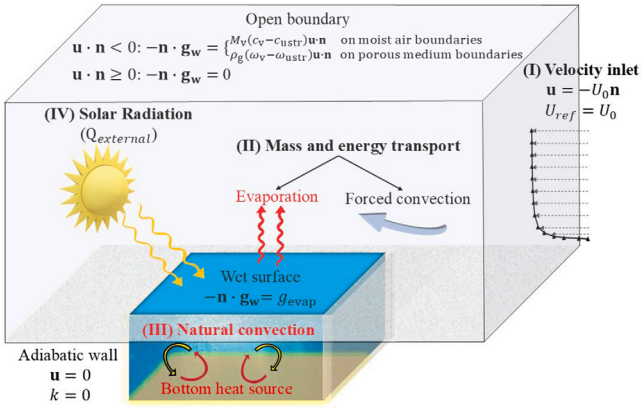

Fig. 1. Physical processes of the open water evaporation.

- The net heat loss of water via surface-to-ambient radiation is considered negligible in comparison to heat loss through convection, as it is largely counterbalanced by the absorption of longwave emissions from the surrounding environment [36].
- The influence of water surface ripples on evaporation is not taken into account, as their effect on average evaporation rates is typically small when compared to dominant factors such as temperature, relative humidity, and wind speed.
- The water level is assumed to remain constant during the simulation, as the short time scale of the analysis results in negligible water loss relative to the total volume [37].
- The vertical and bottom walls of the model are treated as perfectly impermeable and adiabatic [38].
- The initial environmental parameters are established on the basis of fixed baseline values that account for seasonal variations. However, these settings do not adequately consider the continuous temporal changes or phase transitions that may arise due to significant temperature fluctuations.

2.2. Governing equations

The evaporation process of an open-water body can be modeled and analyzed using a set of transient 3-D Navier–Stokes equations combined with evaporation models, as outlined below:

$$\frac{\partial \rho\phi}{\partial t} + \nabla(\rho\vec{v}\phi) = \nabla(\Gamma_\phi \nabla\phi) + S_\phi. \quad (1)$$

The scalar ϕ, diffusion coefficient Γ_ϕ and the source term S_ϕ for the governing equations are specified in Table 1. Both air and water are considered as incompressible fluids, except for the buoyancy-driven flow induced by the density difference, where the Boussinesq approximation is applied. To appropriately determine whether the flow is laminar or turbulent, the bulk Reynolds number (Re) for air and the Rayleigh number (Ra) for water are calculated based on the 3-D geometric configuration and the specified environmental conditions.

- Re number: The Re for airflow under considered windy conditions range from 5.20×10^5 to 1.04×10^6. These calculations assume incompressible air, with constant properties of density 1.184 kg/m^3 and dynamic viscosity 1.82×10^{-5} Pa s at a reference temperature of 25 °C.
- Ra number: The average Ra, determined by the temperature difference between the upper and lower surfaces of the water, fluctuates between 2.0×10^4 and 9.6×10^5. This simulation accounts for variations in the volume expansion coefficient, kinematic viscosity, and Prandtl number of water based on temperature-dependent density.

For external flow over an open-water body, the critical Re is around 5×10^5. The critical Ra for internal nature convection with an aspect ratio of 0.3 is approximately 1×10^4 [39]. Therefore, both air and water flows are modeled as turbulent flows in this study. Consequently, the k-ε model with the incorporation of wall functions is employed for water to accurately simulate near-wall flow dynamics [40]. On the other hand, the low-Re k-ε model, which incorporates damping functions, is employed for forced convection by wind. It effectively predicts flow near the air–water interface, where viscous effects are dominant, while also ensuring accurate representation of turbulence in bulk airflow [41].

The flow fields are then used as input to simulate moisture transport. The turbulent kinetic energy (k) and the dissipation rate of the turbulent kinematic energy (ε) in the standard k-ε model and the low-Re turbulence model are presented in Table 1.

2.3. Boundary conditions, initial conditions and solver

All boundary conditions are prescribed in Fig. 2 and presented in Table 2. For the air domain, the left-hand side is defined as the velocity-inlet boundary to consider the incoming wind, while the other sides and the top surface are defined as open boundaries. The bottom is defined as a wall, except for the air–water interface. For the water domain, all walls are defined as adiabatic surfaces, and external radiation is treated as a heat source applied to the bottom surface of the water domain to simulate solar transmission within the water body [43]. The air–water interface is defined as the node of 'wet surface' (see Section 2.4 for more details). The initial conditions are presented in Table 3, which will be elaborated in Section 3.

The numerical strategy to solve the multiphysics problem is organized into three primary steps. First, the turbulent wind field is solved in a steady-state setting, with the converged solutions subsequently used as inputs for simulating moisture transport within the air domain. Next, a transient simulation is conducted to characterize the heat and mass transfer processes occurring between the water and air domains. During this phase, the phase-change dynamic of evaporation is computed and serves as input for the subsequent moisture transport from water to air. Finally, recognizing the significant influence of natural convection on heat transfer between the top and bottom surfaces of water [44], the transient water flow field is simultaneously simulated during the evaporation process.

In summary, the evaporation process is resolved through several coupling mechanisms. Specifically, airflow is coupled with moisture transport in a unidirectional manner, considering only the effects of turbulent airflow on moisture transport while neglecting any feedback effects. Concurrently, moisture transport in air, forced convection of air, and natural convection of water are coupled for transient calculations. The buoyancy-induced flow in both water and air is modeled using the Boussinesq approximation. The governing equations are discretized using an implicit Backward Differentiation Formula (BDF) time-stepping scheme, which ensures high stability. The resulting linear system matrix is fully coupled and solved using the parallel sparse direct solver PARDISO, known for its speed and robustness.

2.4. Evaporation model

Interfacial evaporation theories at the air–water interface are classified into two primary categories based on their treatment of the interface. The local equilibrium model assumes a continuous temperature across the liquid–gas interface, facilitating a simplified analysis of evaporation. In contrast, the non-equilibrium model incorporates a temperature jump at the interface, rendering it more suitable for phase-change processes where the gas phase is significantly affected by the dynamics of the evaporating interface.

(1) Local equilibrium model

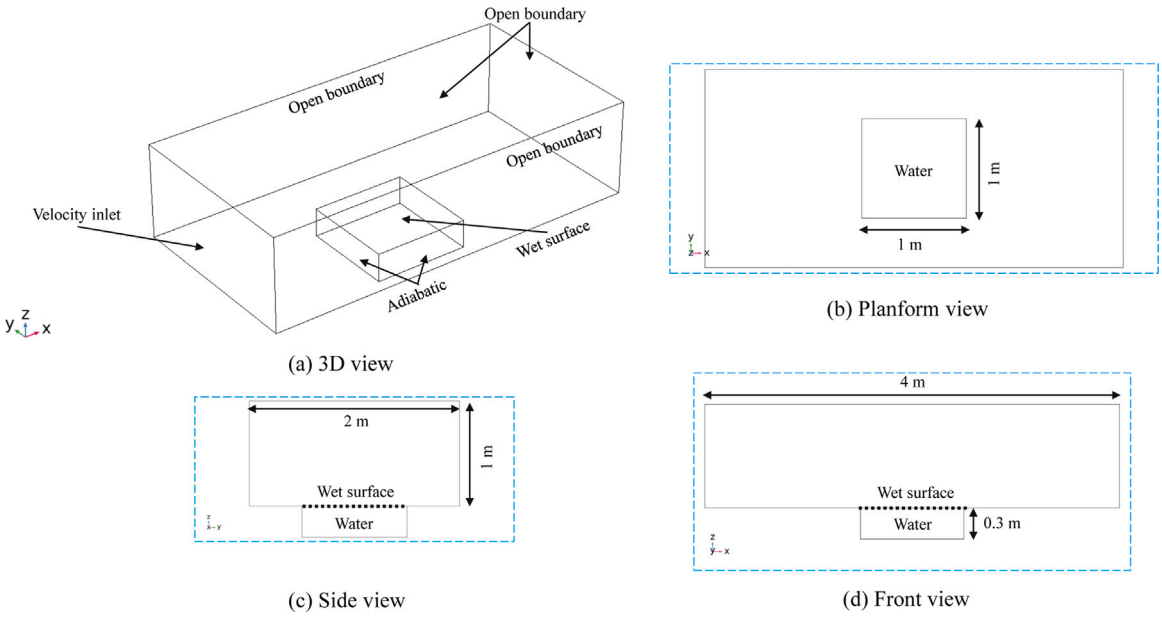

Fig. 2. The boundary conditions and dimensions of the 3-D numerical model at different views, (a) 3-D view, (b) planform view, (c) side view and (d) front view.

Table 1
Summary of governing equations [42].

Equation	ϕ	Γ_ϕ	S_ϕ
Continuity	1	0	0
x-Momentum	U	μ_e	$-\frac{\partial p}{\partial x}+\nabla(\mu_e\frac{\partial}{\partial x}\cdot\vec{v})+F_x$
y-Momentum	V	μ_e	$-\frac{\partial p}{\partial y}+\nabla(\mu_e\frac{\partial}{\partial y}\cdot\vec{v})+F_y$
z-Momentum	W	μ_e	$-\frac{\partial p}{\partial z}+\nabla(\mu_e\frac{\partial}{\partial z}\cdot\vec{v})+\rho_0\beta(T_0-T)g+F_z$
Energy	T	$\frac{K_e}{C_p}$	$\frac{1}{C_p}(\frac{qA_c}{V_c})$
k^*	k	$\mu+\frac{\mu_{t*}}{\delta_k}$	$P_k-\rho\varepsilon$
ε^*	ε	$\mu+\frac{\mu_{t*}}{\delta_\varepsilon}$	$C_{\varepsilon1}\frac{\varepsilon}{k}P_k-C_{\varepsilon2}\rho\frac{\varepsilon^2}{k}$
k^{**}	k	$\mu+\frac{\mu_{t**}}{\delta_k}$	$P_k-\rho\varepsilon$
ε^{**}	ε	$\mu+\frac{\mu_{t**}}{\delta_\varepsilon}$	$C_{\varepsilon1}\frac{\varepsilon}{k}P_k-f_\varepsilon C_{\varepsilon2}\rho\frac{\varepsilon^2}{k}$
where			
$\mu_{t*}=\rho C_\mu\frac{k^2}{\varepsilon}, \mu_{t**}=\rho f_\mu C_\mu\frac{k^2}{\varepsilon}, K_e=K+K_t, K_t=\frac{C_p\mu_t}{Pr_t}$			
$\beta=\frac{1}{T_0}\vert_{P_0}, C_{\varepsilon1}=1.44, C_{\varepsilon2}=1.92, \delta_k=1.0, \delta_\varepsilon=1.44$			
$P_k=\mu_{t2}(\nabla\vec{v}:(\nabla\vec{v}+(\nabla\vec{v})^t)-\frac{2}{3}(\nabla\cdot\vec{v})^2)-\frac{2}{3}\rho k\nabla\cdot\vec{v}$			

* The standard k-ε turbulence model is used for the flow of water.
** The low-Re turbulence model is used for air.

Table 2
Detailed expressions of the boundary conditions.

Fluid	Type of boundary	k	ε
Air	Velocity Inlet	$\frac{3}{2}(U_T I_T)^2$	$C_\mu^{3/4}\frac{k^{3/2}}{L_T}$
Air	Open boundary	$\frac{3}{2}(U_{\text{ref}} I_T)^2$	$C_\mu^{3/4}\frac{k^{3/2}}{L_T}$
Air	Wall	0	$\lim_{\ell_w\to0}\frac{2\upsilon k}{\ell_w^2}$
Water	Wall	$\nabla k\cdot n=0$	$\rho\frac{C_\mu k^2}{\kappa_\upsilon\delta_w^+\mu}$

I_T: Turbulence intensity (%).
L_T: Turbulence length scale (m).
δ_w^+: Lift-off from the physical wall.
κ_υ: The von Kármán constant.

The local equilibrium model posits a smooth temperature transition from liquid to gas at the air–water interface while permitting a discontinuity in heat flux due to latent heat absorption or release [45]. During the evaporation process, water vapor diffuses into the surrounding air, establishing a moisture concentration gradient that governs the evaporation rate. This model treats the transport of water vapor as diffusion-driven, employing Fick's law to calculate the vapor mass flux. Given the substantial density difference between liquid water and vapor, the generated vapor creates a velocity discontinuity at the interface, thereby inducing Stefan flow [46]. This Stefan flow, which is proportional to the evaporation rate, counteracts the diffusion of air toward the interface. Consequently, the evaporation flux, g_{evap}, is defined as the sum of both diffusive and convective vapor transports.

$$g_{evap} = M_v K(c_{sat} - c_v) + u_{\text{stefan}}\,\rho_g, \tag{2}$$

where M_v is the molar mass of water vapor, K is the initial evaporation rate factor, $c_{sat} = p_{sat}/(R_g T)$ is the saturated concentration of vapor, c_v is the vapor concentration, u_{stefan} is the Stefan flow velocity and ρ_g is the moisture density.

(2) Non-equilibrium model

In the non-equilibrium model for liquid–vapor systems, two micro-scale layers develop between the bulk phases of water and vapor: the interfacial transition layer and the Knudsen layer. Within the transition layer, the liquid density gradually transitions to vapor density, resulting in a subtle yet discontinuous temperature jump. The Knudsen layer, characterized by significant molecular interactions, can exhibit pronounced temperature variations. Due to the discontinuities in density,

pressure, and temperature, traditional continuity principles are inadequate for modeling vapor transport within the Knudsen layer. Instead, Molecular Kinetic Theory (MKT) provides a framework to describe the phase-change mass flux at the air–water interface, accounting for variations in macroscopic quantities driven by molecular interactions.

$$J = \frac{2\lambda}{2-\lambda}\sqrt{\frac{1}{2\pi R_v}}\left[\frac{p_s(T_i)}{T_i^{1/2}} - \frac{p_v}{T_v^{1/2}}\right], \tag{3}$$

where λ is the accommodation coefficient, p_v and T_v denote the partial pressure and temperature on the vapor side of the Knudsen layer, respectively, while the subscript s represents the saturation value of steam and i for the interfacial value.

Both local equilibrium and non-equilibrium models have been validated against experimental data, showing strong capabilities for water evaporation calculations [47]. However, the non-equilibrium model excels in providing insights into the molecular dynamics of evaporation but faces limitations due to the need for adjustable coefficients that link the theoretical model to empirical data, introducing uncertainties. Therefore, the local equilibrium model is chosen in this work due to its relative simplicity and robustness.

In an open-water body where the air domain is significantly larger than the water surface, and under the influence of wind, the moisture can be assumed to be dilute. This means that the moisture density remains nearly constant as a result of the low concentration of vapor. Therefore, changes in water content are primarily reflected through variations in vapor concentration,

$$M_v\frac{\partial c_v}{\partial t} + M_v u\cdot\nabla c_v + \nabla\cdot g = G. \tag{4}$$

Under this assumption, the Stefan flow generated by a low concentration of water vapor under outdoor conditions can be neglected. Therefore, the evaporation rate of the open-water body can be simplified as Eq. (5), which is the mathematical definition of 'wet surface' in COMSOL Multiphysics.

$$g_{evap} = -M_v\left(\frac{\mathrm{Sh}\cdot D_{VA}}{L}\right)\cdot\frac{P_{sat}(T)}{RT}\cdot(1-RH), \tag{5}$$

where D_{VA} represents the mass diffusion coefficient, with a value of 2.6×10^{-5} m^2 s^{-1} for air–vapor, while L denotes the characteristic length, R is the gas constant and Sh is the Sherwood number.

In quiescent air conditions, water vapor distribution is primarily governed by molecular diffusion. Therefore, calculations based on the saturation concentration difference may not accurately estimate the evaporation rate. Instead, the vapor transport should be determined based on the concentration gradient, as shown in Eq. (6), which is the general expression of vapor diffusive flux.

$$g_{evap} = -M_v D_{VA}\nabla c_v. \tag{6}$$

To evaluate the impact of neglecting the Stefan flow, we conducted simulations under two conditions: one that incorporates the Stefan flow and another that excludes it, as depicted in Fig. 3. The results reveal that while evaporation rates are consistently lower when the Stefan flow is not considered, the maximum discrepancy observed after an 8-h simulation is less than 5%. Consequently, to simplify the calculations without compromising accuracy, future simulations will not consider the Stefan flow.

Lastly, the latent heat source q_{evap} is determined by multiplying the evaporation flux by the latent heat of evaporation h_{fg},

$$q_{evap} = h_{fg}g_{evap}. \tag{7}$$

Before presenting reliable results, a thorough examination of grid independence, time step selection, and validation of numerical strategies is conducted, as detailed in Appendix. All simulations are performed on a Windows Server (x64) equipped with an AMD Ryzen Threadripper 3970X 32-core processor and 128 GB of RAM.

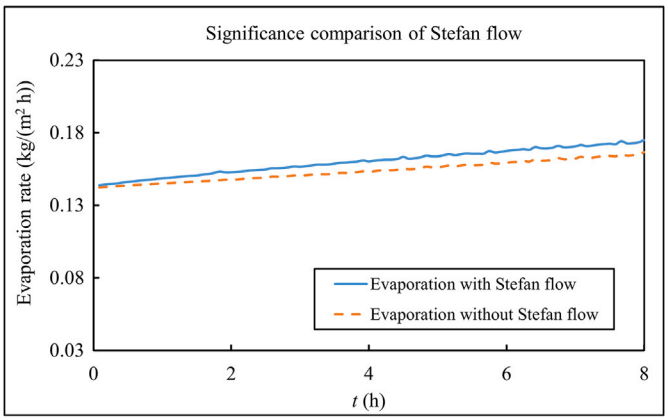

Fig. 3. The effect of Stefan flow on the evaporation rate under summer environmental conditions with 2 m/s wind speed.

Table 3
Summary of typical environmental conditions in four different seasons.

	Autumn/Spring	Summer	Winter
Air temperature	20 °C	35 °C	5 °C
Water temperature	20 °C	30 °C	10 °C
Relative humidity	50%	70%	30%
Wind speed	0, 2, 5 m/s	0, 2, 5 m/s	0, 2, 5 m/s
Heat input (if exists)	884 W/m^2	884 W/m^2	884 W/m^2
Heat input position	Bottom	Bottom	Bottom

3. Results and discussion

As discussed in Section 1, the previous literature has extensively discussed the effects of relative humidity, temperature, and wind speed on water evaporation, both theoretically and experimentally [8,10,11]. In this study, we investigate the crucial impacts of natural convection within an open-water body on evaporation, a facet often simplified in prior research. To this end, we conducted simulations under four distinct seasonal conditions, each characterized by combinations of relative humidity, air temperature, and initial water temperature.

Considering the different specific heat capacities of air and water, we make a reasonable assumption: the initial temperature of the water body is 5 °C lower than the air temperature in summer, 5 °C higher in winter and equivalent in autumn and spring [48]. These conditions reflect typical days in the four different seasons, which are summarized in Table 3. Wind speed varies from 0 m/s (windless) to 2 m/s (moderate wind) and up to 5 m/s (strong wind). To mimic the propagation and absorption of solar radiation within the water body [43], a constant surface heat flux of 884 W/m^2 is applied to the bottom surface of the water body from $t = 0$ until the end of the simulation. Furthermore, scenarios without heat input, such as during nighttime or on cloudy days, will also be investigated for comparison, while all other conditions remain unchanged.

3.1. Effects of natural convection within an open-water body on water evaporation

The buoyancy-driven flow within an open-water body has been shown to play a significant role in its internal circulation [40]. However, its further impacts on water evaporation have not been thoroughly investigated. Consequently, we conducted a comparative study between cases that include convection effects on evaporation, referred to as the convection-present case, and those that exclude these effects, referred to as the convection-free case. In reality, it is impractical to only consider conduction effects within an open-water body, as whenever there is a temperature difference within the water body, natural convection is inevitably initiated. However, to quantify its

effect, we simulate a scenario in which conduction is the sole heat transfer mechanism, by disregarding the thermal expansion of water in COMSOL Multiphysics.

Note that this work focuses specifically on the effects of natural convection within an open-water body on water evaporation. Therefore, existing conclusions about the relationship between evaporation and factors such as relative humidity, air, or water temperature are not reiterated with emphasis.

3.1.1. With external heat source

First, the comparative results of water evaporation rates with external heat input for convection-present and convection-free cases under both windless and windy conditions are illustrated in Fig. 4. Under windless conditions, the time-varying evaporation rates of convection-free cases exhibit a consistent decrease throughout all seasons. For example, the value decreases from 0.0035 to 0.001 kg/(m^2 h) during autumn and spring. In contrast, for convection-present cases, the evaporation rates initially decrease, then gradually increase until the end of the calculation period. The corresponding value decreases from 0.0035 to 0.002 kg/(m^2 h), then increases to 0.0025 kg/(m^2 h) during autumn and spring. When comparing both predictions, the average evaporation rate of the convection-present cases is more than three times higher than that of convection-free cases under windless conditions. In the presence of wind, the time-varying evaporation rates for convection-free cases continue to decrease, whereas those for convection-present cases exhibit a steady increase. However, as the wind speed increases from 2 to 5 m/s, the rate of increase (decrease) in evaporation for convection-present (convection-free) cases diminishes. For instance, during autumn and spring, the evaporation rate for the convection-present case increases from 0.165 to 0.171 kg/(m^2 h) at a wind speed of 2 m/s and from 0.615 to 0.620 kg/(m^2 h) at 5 m/s. In contrast, the evaporation rate for the convection-free case decreases from 0.165 to 0.056 kg/(m^2 h) at 2 m/s and from 0.615 to 0.390 kg/(m^2 h) at 5 m/s. In addition, the evaporation rate of convection-present cases is approximately 2.5 times higher than that of convection-free cases at a wind speed of 2 m/s and about 1.5 times higher at 5 m/s.

Second, a comparison of the time-varying evaporation rates in windless and windy conditions reveals consistent and inconsistent trends. Consistent observations include the monotonically decreasing trend in evaporation rates for convection-free cases, transitioning from rapid to gradual declines throughout the calculation period, regardless of the season. In contrast, convection-present cases exhibit diverse patterns. Under windless conditions, evaporation rates initially decrease before reversing to an upward trend, whereas under windy conditions, the rates consistently increase over time. Furthermore, in response to seasonal variations, the evaporation rate in summer starts at its lowest point and rises to become the highest at the end of the calculation period under windless conditions. However, the introduction of wind maintains the summer evaporation rate between those observed in autumn/spring and winter.

Finally, the evaporation rates for convection-present cases with no external heat input (referred to as external-heat-free cases) are presented under both windless and windy conditions in Fig. 4. Specifically, under windless conditions, the evaporation rates exhibit an initial sharp decline, followed by a transition to a more gradual decrease. For example, the evaporation rate for the external-heat-free case during autumn and spring decreases from 0.0035 to 0.0011 kg/(m^2 h), which is slightly higher than that of the convection-free case. In terms of the value of evaporation rates under different seasons, it is highest in autumn/spring, followed by winter, and then summer under windless conditions. In contrast, under windy conditions, the evaporation rates remain relatively constant over time. And the evaporation rate ranks highest in autumn/spring, followed by summer, and then winter.

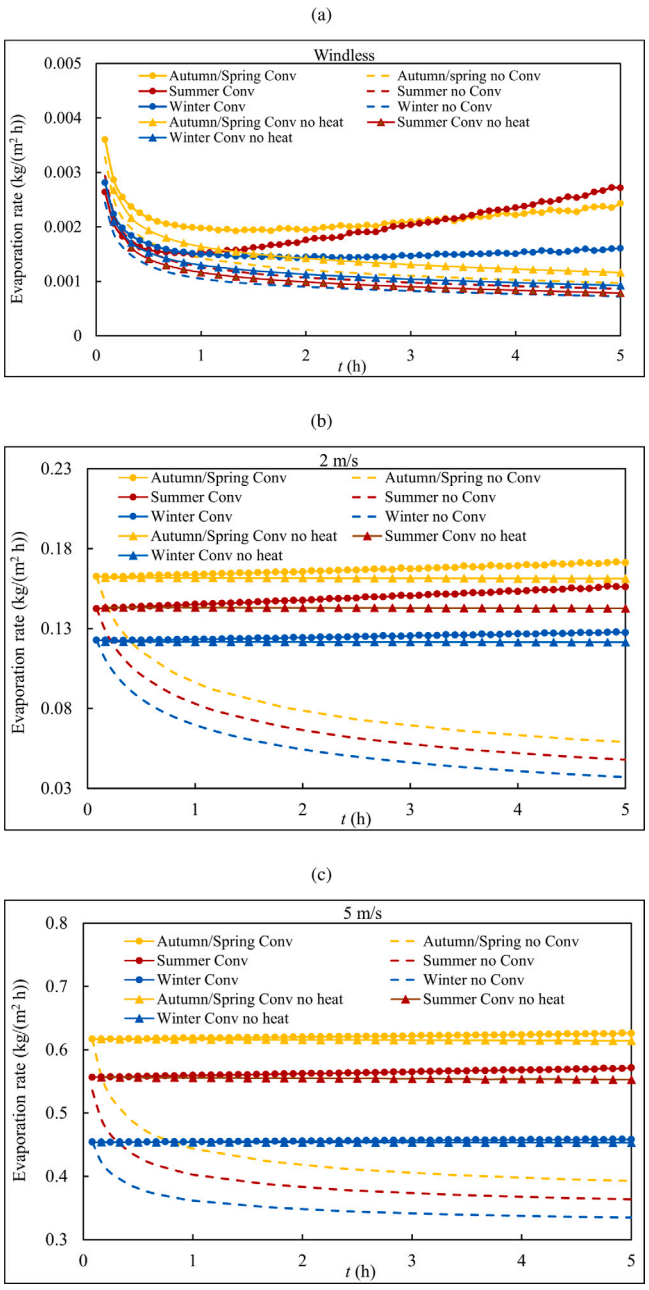

Fig. 4. Time-varying evaporation rate under different wind conditions (a) windless, (b) 2 m/s and (c) 5 m/s with convection and external heat (—•—), with convection but without external heat (—▲—) and without convection and external heat (– – –).

3.1.2. Without external heat source

Compared to convection-present cases with external heat, the absence of external heat leads to distinct differences in the time-varying evaporation rates under both windless and windy conditions, even when accounting for natural convection within the open-water body. Specifically, under windless conditions, the evaporation rate of the convection-present case during summer is initially lower than that of the other three seasons; however, it gradually increases and ultimately surpasses the rates observed in autumn/spring and winter. Conversely, the evaporation rate of the external-heat-free case in summer remains consistently lower than those recorded in autumn/spring and winter. In windy conditions, the evaporation rates of external-heat-free cases across different seasons exhibit different behavior compared to those of convection-present cases with external heat input. While the

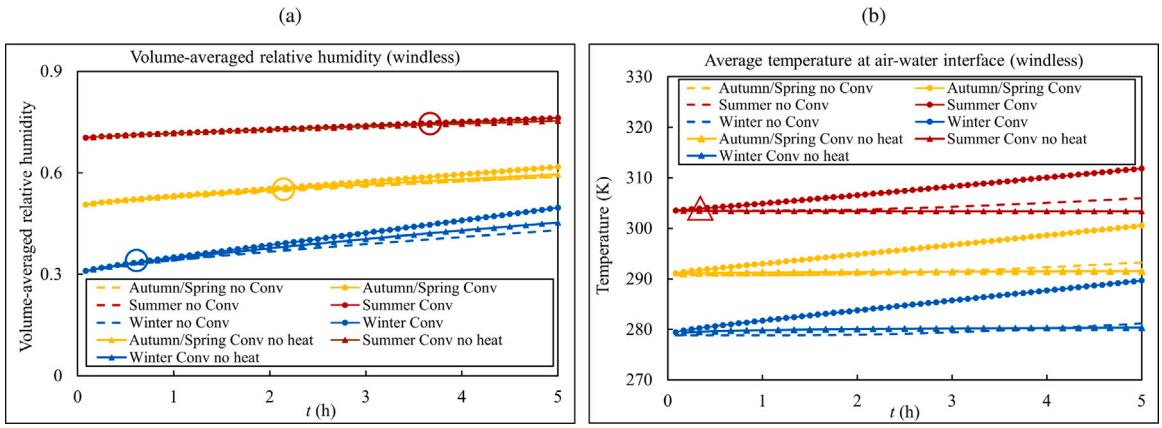

Fig. 5. The time-varying volume-averaged relative humidity and temperature at air–water interface under windless condition.

evaporation rates with external heat input continue to rise throughout the simulation, the absence of external heat leads to a consistently decreasing evaporation rate during the same period. As wind speed increases, the evaporation rates for cases with and without external heat input converge across all seasonal conditions. Specifically, the average evaporation rate of convection-present cases is approximately 2 times higher than that of external-heat-free cases under windless conditions, and about 1.05 times and 1.02 times higher at wind speeds of 2 m/s and 5 m/s, respectively.

Based on the findings presented, it can be inferred that the evaporation rate of an open-water body is influenced by the presence of natural convection, as well as the intensity of that convection within the water body (with and without external heat source).

3.2. Mechanisms of the impacts of natural convection on water evaporation

To elucidate the role of natural convection within the water body in evaporation, the findings are analyzed by presenting the distributions of temperature, relative humidity, and flow instability (Rayleigh–Bénard convection roll pattern).

3.2.1. In windless condition

Under windless conditions, as indicated by Eq. (5), evaporation is initially driven by the difference in saturated vapor concentration at the air–water interface and air vapor concentration. The time-varying temperature at the interface and volume-averaged relative humidity of the surroundings are illustrated in Fig. 5, in which convection-present, convection-free and external-heat-free cases are compared. The volume-averaged relative humidity of air accumulates and increases over time in the four seasons. Notably, the relative humidity for convection-present cases exceeds that for convection-free and external-heat-free cases after specific time points in each season ($t = 2.1$ h in autumn/spring, $t = 3.8$ h in summer and $t = 0.7$ h in winter) due to different initial relative humidity values (that is, 0.5 in autumn/spring, 0.7 in summer and 0.3 in winter). Before those points, the volume-averaged relative humidity for all cases is nearly identical. In addition, the time-varying relative humidity for convection-free and external-heat-free cases is similar, except for that in winter. Fig. 6 shows the contours of relative humidity in summer, revealing the accumulation of moist air near the interface, which gradually hinders the evaporation of water in the air. It can also be observed that the cases with convection exhibit a greater accumulation of vapor over time compared to the other two cases, which show similar accumulation levels.

Meanwhile, in terms of the temperature for the air–water interface, it continuously rises in convection-present cases, contributing to a sustained increase in saturated vapor pressure, while for convection-free cases, it remains constant for two hours then gradually increases. As a comparative study, the interface temperature for the external-heat-free cases keeps decreasing slowly during the simulation.

Based on the analysis above, we can infer that the evaporation rate of an open-water body under windless conditions is influenced by two main factors: (1) the accumulation of moist air above the air–water interface, and (2) the increasing temperature of the air–water interface. Rewriting Eq. (5) as $g_{evap} = M_v K(1 - RH)c_{sat}$ based on $RH = c_v/c_{sat}$, we can conclude that the first factor c_v slows down the water evaporation rate, while the second factor c_{sat} accelerates it. Thus, the evaporation process under windless conditions can be divided into two stages: (1) accumulation of moist air above the air–water interface with a slightly increasing temperature at the interface and (2) continuous accumulation of moist air above the interface with an obviously increasing temperature at the interface. This explains why the evaporation rates for both the convection-free and external-heat-free cases decrease steadily over time. The initial driving force from the vapor pressure difference diminishes due to the accumulation of water vapor, and there is no increase in temperature at the air–water interface to facilitate further evaporation. In contrast, for convection-present cases, the patterns of water evaporation (initial decrease followed by an increase, as shown in Fig. 4(a)) indicate that the initial decline in evaporation rate is primarily driven by a decrease in the relative humidity difference. Subsequently, the increase in evaporation is dominated by the increasing temperature difference between the interface and the ambient environment. In addition, the evaporation rate of convection-free cases remains consistently lower than that of convection-present cases in all seasons. These trends align with the time-varying temperatures of the air–water interface (Fig. 5(b)). The finding could be cross-validated by the external-heat-free cases, the evaporation rate initially decreases due to the accumulation of moisture and drops continuously as no external heat input to maintain the temperature at the air–water interface.

How does the natural convection of water keep the temperature at the air–water interface higher in autumn/spring and winter, but first equivalent and then higher in summer, when compared with convection-free cases? To elucidate the underlying mechanisms, the temperature contours of the water body at different time points are presented in Figs. 7 and 8, comparing convection-present and convection-free cases in winter and summer, respectively. In Fig. 7, where the initial water temperature is 5 °C higher than the air temperature in winter, noticeable differences in temperature contours are observed between convection-present and convection-free cases at various time points. Generally, when natural convection is considered within the water body, the temperature distribution rapidly becomes uniform. However, in convection-free scenarios, the temperature gradually decreases from layer to layer, with a slower heat transfer rate. In both cases, a distinct temperature gap is evident between the water body and the air near the interface. For convection-present cases, the faster heat

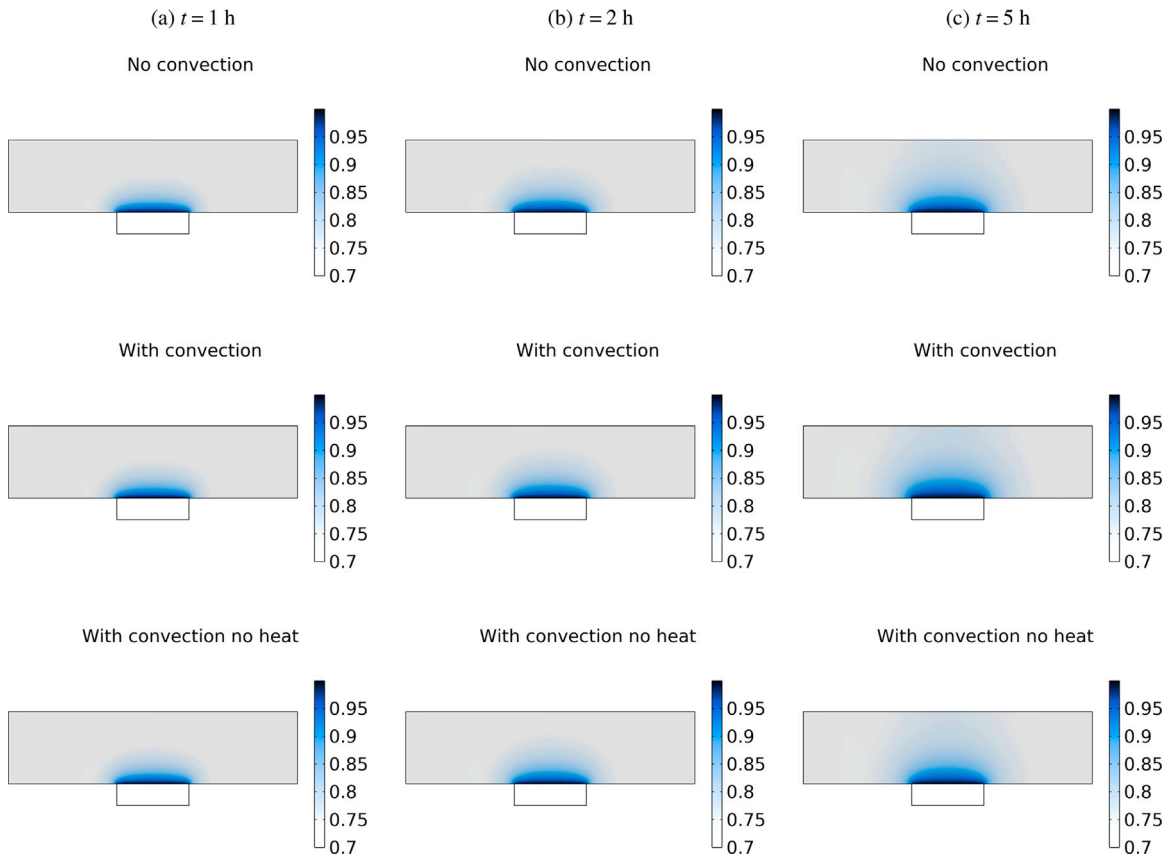

Fig. 6. The relative humidity distribution at different times in summer under windless condition.

transfer speed induced by natural convection within the water body results in a temperature gradient that decreases from the bottom to the top layers. Moreover, the latent heat of water evaporation contributes to lower temperatures above the air–water interface, particularly in the middle areas. These areas do not have contact with ambient air that has a higher temperature, while the peripheral areas can absorb heat as a result of direct contact. In convection-free cases, similar but weaker trends are observed, indicating reduced heat transfer within the water body and from water to air. Consequently, the initial temperature at the air–water interface is lower in convection-free cases than in convection-present cases. Moreover, over time, the natural convection effect facilitates more efficient heat transfer from the bottom to the top layers in convection-present cases, resulting in a progressively greater temperature difference at the top surface compared to that in convection-free cases.

In contrast, during summer, when the initial air temperature is 5 °C higher than the water, the time-varying temperature distribution differs for convection-present and convection-free cases (Fig. 8). At $t = 5$ min, a similar temperature distribution is observed for both cases. However, as time progresses to $t = 2$ h and to $t = 5$ h, the water temperature increases for the convection-present case, leading to a temperature increase at the air–water interface despite the accumulation of moist air above. Conversely, for the convection-free case, because of the absence of natural convection within the water body, it takes longer for the water surface temperature to exceed the ambient temperature. Both cases exhibit a similar evaporation rate until the water temperature exceeds the ambient temperature, after which the difference becomes apparent.

The significance of natural convection within an open-water body for the temperature dynamics at the air–water interface has been clearly identified. To further elucidate the evolution of heat transfer and flow instability within the open-water body, we analyze the dimensionless Rayleigh number and the corresponding roll patterns. As illustrated in Fig. 9, the time-varying Rayleigh number for the open-water body is presented for both convection-present and external-heat-free scenarios during summer and winter under windless conditions.

Notably, the Ra exhibits an increasing trend with oscillations under continuous heating, whereas it shows a slight decrease over time in the absence of external heat input. The difference between the convection-present case and the external-heat-free case occurs after 20 min in summer and 1 h in winter. Specifically, as discussed in Section 2.2, the critical Ra is around 1×10^4, which is marked as the dashed lines in Fig. 9. This observation indicates that the flow within the open-water body transitions from laminar to turbulent after 1 h of external heat input during summer. In the absence of external heat, the flow remains laminar throughout the period. In winter, the water flow rapidly shifts from laminar to turbulent after around 20 min regardless of external heat input; however, the intensity of the turbulence increases gradually with the application of external heat.

Furthermore, Ra for the convection-present case during summer exhibits a more pronounced increase compared to the winter cases. In contrast, Ra for the external-heat-free case in summer is consistently lower than that recorded in winter. As illustrated in Fig. 5, the temporal variations in temperature at the air–water interface display patterns that are analogous to those observed in Ra, regardless of season.

To visualize the time-varying temperature at the air–water interface, we examined the evolution of the roll pattern in the open-water body during summer, considering both the convection-present case and the external-heat-free case at various time points and Ra, as illustrated in Figs. 10 and 11. This study was conducted following a comparative validation against experimental data to ensure accuracy and reliability (see Figs. A8, A9 and Table A.4). Observations were made from both the top and side views of the open-water body. In the convection-present

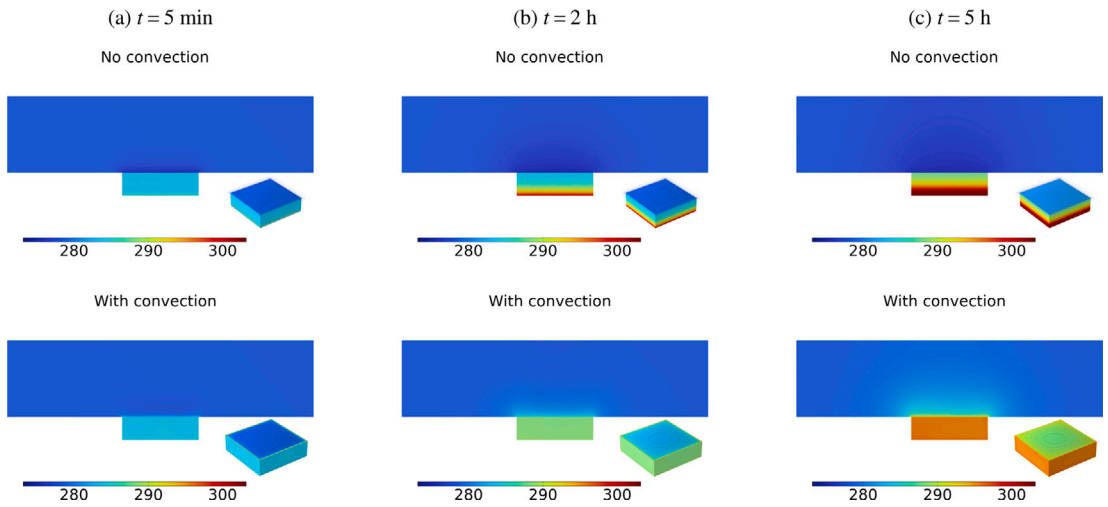

Fig. 7. The temperature distribution at different times in winter under windless condition.

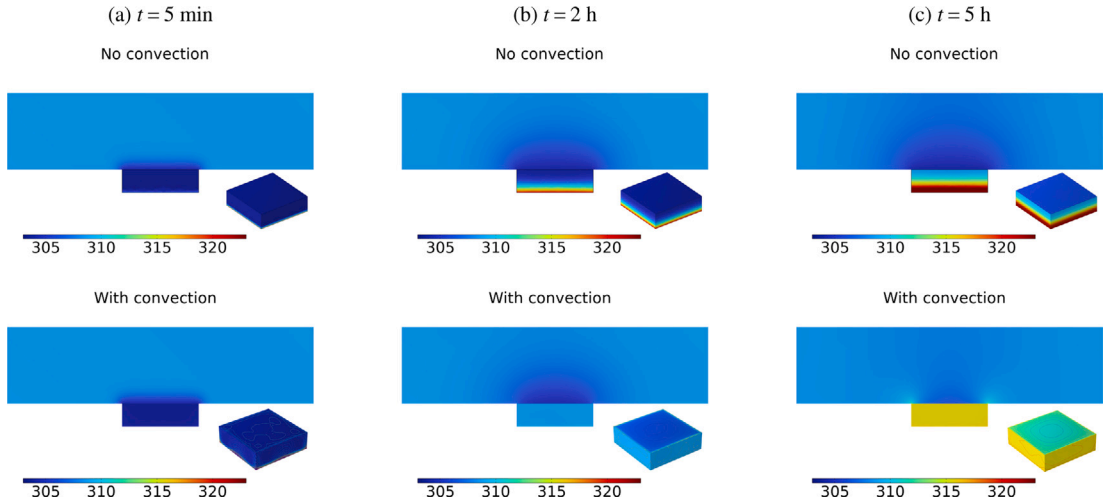

Fig. 8. The temperature distribution at different times in summer under windless condition.

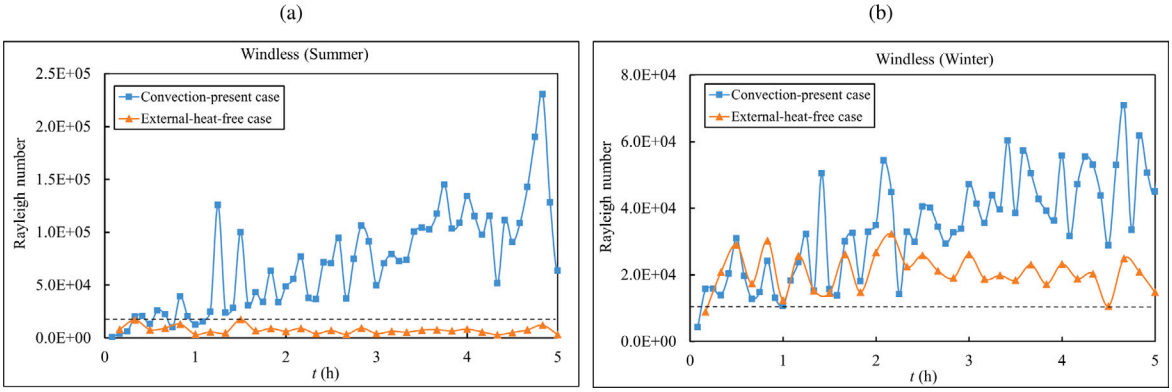

Fig. 9. The time-varying Rayleigh number for the open-water body is presented for both convection-present and external-heat-free scenarios during summer and winter under windless conditions.

case, the flow exhibits chaotic behavior, with heat being transported from the bottom to the top by two distinct rolling cells (see Fig. 10(a)). After 0.5 h, one of the rolling cells begins to grow larger than the other, resulting in a warmer region forming between the two cells (Fig. 10(b)). As time progresses, the larger cell becomes dominant in heat transfer, then ultimately merging with the smaller cell. Despite the instability of the flow pattern, the overall configuration remains relatively unchanged between the 2-h and 5-h time instants. In contrast, the external-heat-free case maintains a consistent roll pattern throughout the entire observation period. Specifically, two opposing rolling cells are evident from the side view, creating a relatively warm region in the center of the open-water body. The differences between

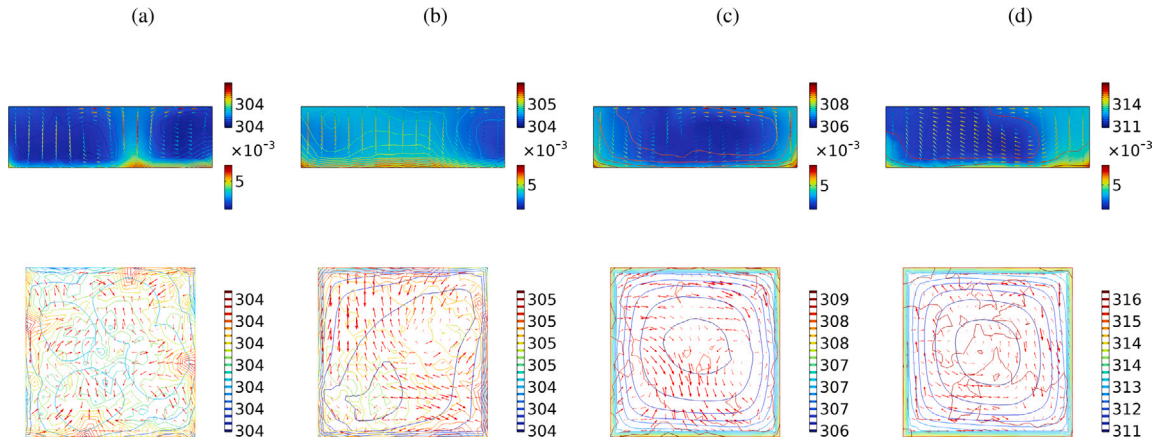

Fig. 10. The side and top views for the roll pattern of water for convection-present case under windless condition, (a) $t = 10$ mins, Ra $= 3.9 \times 10^3$, (b) $t = 0.5$ h, Ra $= 1.3 \times 10^4$, (c) $t = 2$ h, Ra $= 4.8 \times 10^4$, (d) $t = 5$ h, Ra $= 6.4 \times 10^4$.

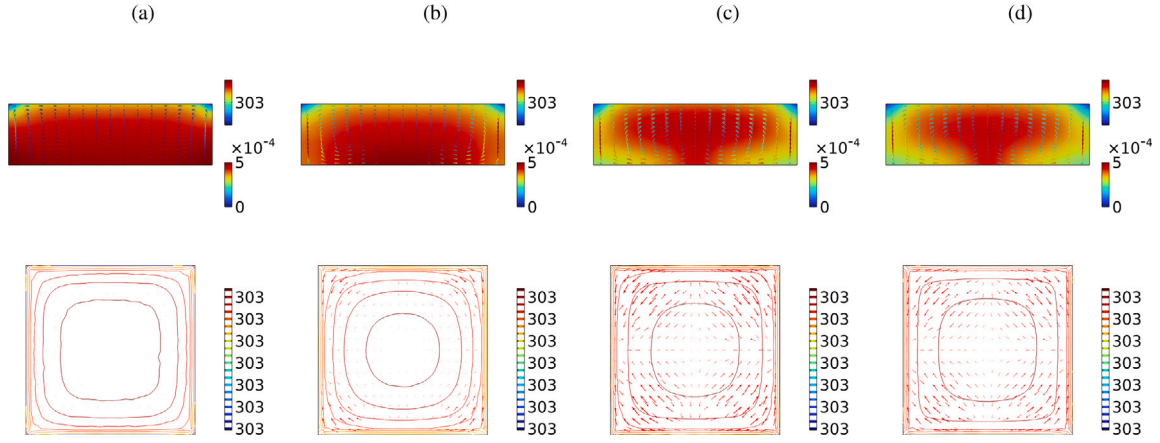

Fig. 11. The side and top views for the roll pattern of water for external-heat-free case under windless condition, (a) $t = 10$ mins, Ra $= 8.2 \times 10^3$, (b) $t = 0.5$ h, Ra $= 7.8 \times 10^3$, (c) $t = 2$ h, Ra $= 6.4 \times 10^3$, (d) $t = 5$ h, Ra $= 3.2 \times 10^3$.

the two cases are notable: in the convection-present case, the roll pattern is consistently chaotic, while in the external-heat-free case, the roll pattern remains stable throughout the observation period. Additionally, the convection-present case begins with several smaller cells that eventually coalesce into a single large cell, which matches the scale of the open-water body. In contrast, the external-heat-free case starts with a large cell and maintains this configuration consistently over time.

Considering Figs. 5(b) and 8, it is evident that the flow in the open-water body with external heat input is unstable, and this chaotic behavior facilitates the transition from laminar to turbulent flow, thereby gradually enhancing heat transfer efficiency. Ultimately, the system evolves into a single large cell, which is the most efficient configuration for transporting heat from the bottom to the top, increasing the temperature at the air–water temperature. By contrast, in the absence of external heat input, the flow begins as weakly laminar, characterized by low heat transfer efficiency, yet it can maintain a consistent roll pattern as well as stable temperature at the air–water interface.

3.2.2. *In windy condition*

It is evident in Fig. 4 that the changing trends of evaporation in convection-free cases resemble those under windless conditions when wind is introduced. This is because forced convection of the wind decreases the temperature at the air–water interface, while keeping other ambient conditions unchanged, including relative humidity and air temperature. In contrast, the changing trends of evaporation for convection-present cases deviate from those under windless conditions. As depicted in Fig. 4, the evaporation rate increases monotonically during the calculation period, rather than initially decreasing and subsequently increasing. When examining the volume-averaged relative humidity at the air–water interface under 2 m/s and 5 m/s windy conditions as shown in Fig. 12, it remains nearly constant in both windy conditions, contrasting with the windless condition. Meanwhile, the interface temperature exhibits a monotonic increase trend for convection-present cases regardless of seasons. Considering Fig. 4(b) and (c), it can be inferred that the temporal evolution of the evaporation rate in an open-water body is determined solely by the temperature at the air–water interface under windy conditions.

In addition, the heat transfer process within the open-water body is analyzed, as illustrated in Figs. 13 and 14, where the air flows from left to right. For the convection-present case, the evolution of the roll pattern in the water differs significantly with the presence of wind, regardless of external heat input. Specifically, when external heat is applied, the initial roll pattern consists of two cells: a clockwise cell on the right-hand side and an anticlockwise cell on the left-hand side (Fig. 13(a)), similar to the windless scenario. However, the roll pattern gradually evolves into a larger clockwise cell after 5 h, contrasting with the windless case, which develops into a large anticlockwise cell. In addition, the presence of wind complicates the temperature distribution at the air–water interface, resulting in a more heterogeneous pattern. In contrast, without wind, the temperature distribution at the air–water interface is relatively orderly, exhibiting a gradient that warms from the center to the periphery.

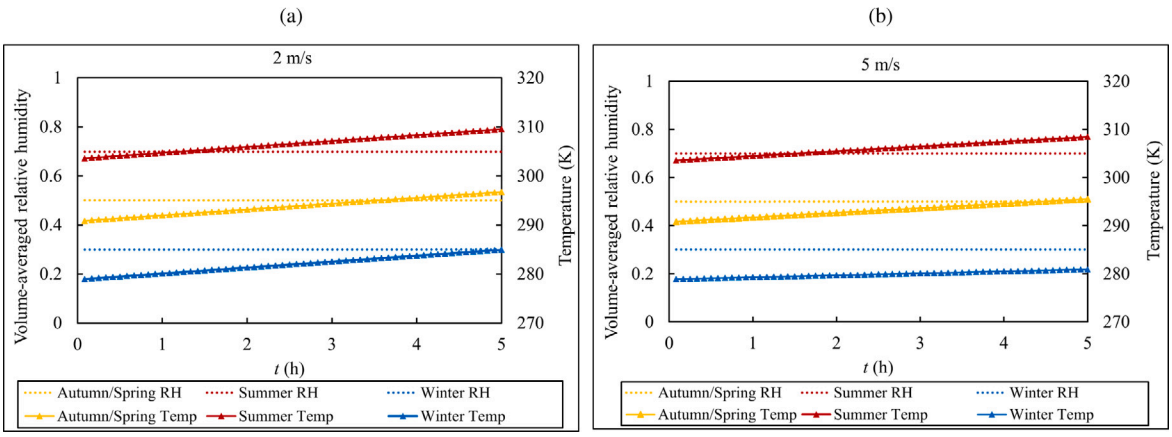

Fig. 12. The time-varying volume-averaged relative humidity of ambient air and temperature at air–water interface at (a) 2 m/s and (b) 5 m/s.

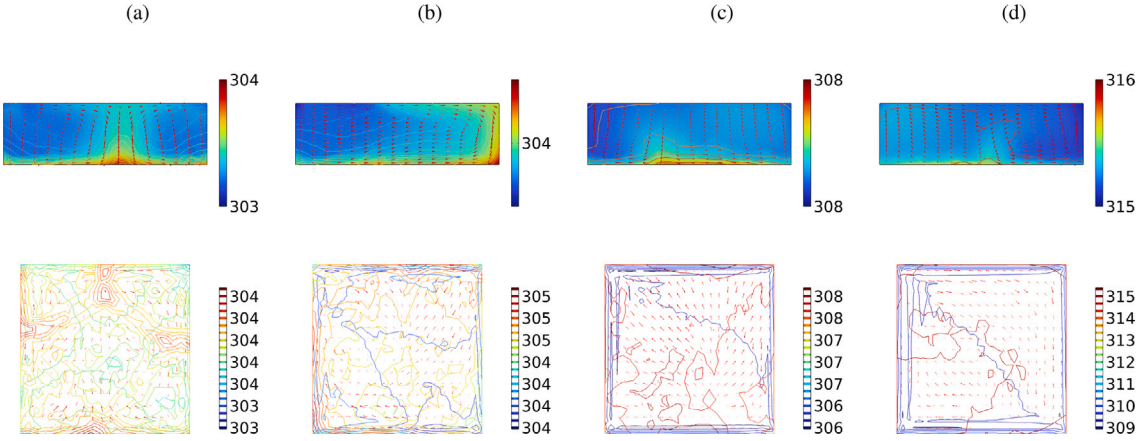

Fig. 13. The side and top views for the roll pattern of water for convection-present case under 2 m/s wind condition, (a) t = 10 mins, Ra = 2.2×10^3, (b) t = 0.5 h, Ra = 1.3×10^4, (c) t = 2 h, Ra = 9.9×10^4, (d) t = 5 h, Ra = 1.1×10^5.

In the absence of external heat input, wind disrupts the stable roll pattern of the water. Specifically, as the wind blows from left to right, a lower temperature region forms in the upper left area. This cooler region has a larger density and sinks along the left-hand side wall, creating an anticlockwise rolling cell. In the windless scenario, two lower temperature regions develop in both upper left corners, and the sinking of higher-density water from the side walls leads to the formation of two symmetrical cells, as previously described.

Therefore, the roll pattern under windy conditions results from the combined effects of forced convection in air and natural convection in water arising from temperature differences. Despite the change in the direction of the roll pattern caused by the wind, the overall evolution still progresses from several smaller cells to a larger one. This indicates that while forced convection from the wind alters the direction of the roll pattern, natural convection driven by external heat input governs the evolution of the roll pattern. However, in the absence of external heat input, the roll pattern is predominantly influenced by forced convection of the wind, which disrupts the ordered rolling cells observed under windless conditions.

4. Conclusions

In this work, we developed a comprehensive 3-D multiphysics numerical model using COMSOL Multiphysics to investigate the significance of natural convection within an open-water body on water evaporation. The contributions are:

(1) Development of the numerical model: The developed 3-D numerical model accounted for all physical phenomena during the water evaporation process. Validation against scale models of both indoor and outdoor swimming pools from existing literature confirms that the model exhibits a high degree of accuracy in replicating experimental results.

(2) Quantification of the significance of natural convection: We revealed that neglecting natural convection within an open-water body results in significant discrepancies in estimating the time-varying evaporation rate. Specifically, the evaporation rate in cases with natural convection is more than 2.5 times greater in windless conditions, 2.5 times greater with a wind speed of 2 m/s and 1.5 times greater with 5 m/s wind, when compared to convection-free scenarios. This discrepancy arises from the lower heat transfer rate of pure conduction compared to natural convection.

(3) Identification of the determinants of the evaporation rate of an open-water body: Under windless conditions, the evaporation rate is initially influenced by the accumulation of moist air and subsequently affected by the temperature of the air–water interface. In contrast, the temperature at the air–water interface serves as the sole factor determining the evaporation rate of an open-water body under windy conditions.

In summary, the developed 3-D numerical model, along with simulations conducted under various environmental conditions – focusing on internal natural convection within the water body – significantly extends the range of validity beyond previous empirical correlations and accurately reproduces the physical phenomena observed in field experiments at a lower cost. Unlike empirical correlations and experimental approaches, our model offers practical applicability to improve water management strategies in outdoor ponds, irrigation systems, and industrial cooling processes.

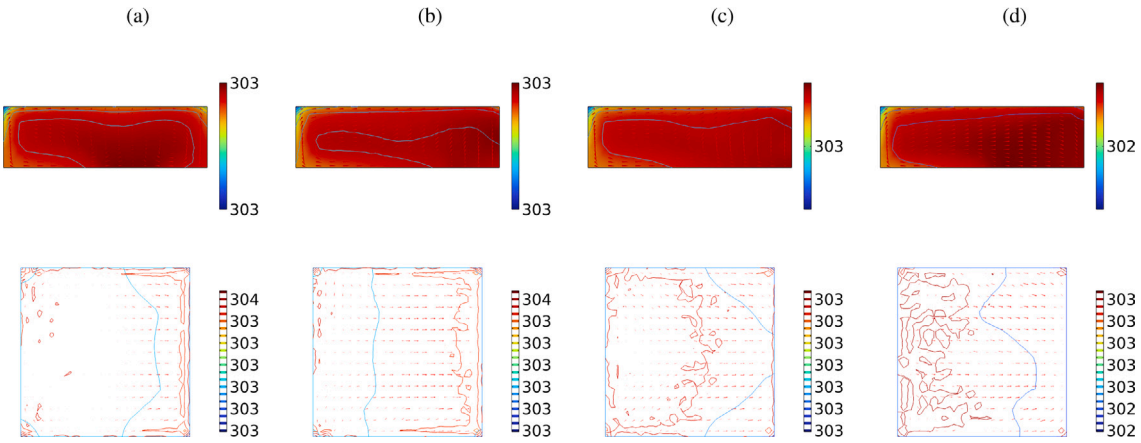

Fig. 14. The side and top views for the roll pattern of water for external-heat-free case under 2 m/s wind condition, (a) t = 10 min, Ra = 7.2×10^2, (b) t = 0.5 h, Ra = 9.8×10^3, (c) t = 2 h, Ra = 6.9×10^3, (d) t = 5 h, Ra = 5.0×10^3.

CRediT authorship contribution statement

Peixin Dong: Writing – original draft, Validation, Software, Methodology, Investigation. **Haoran Chang:** Writing – original draft, Software, Methodology, Investigation. **Nan Deng:** Writing – review & editing, Methodology, Data curation. **Su Guo:** Writing – review & editing, Resources, Funding acquisition. **Mengying Li:** Writing – review & editing, Project administration, Funding acquisition, Conceptualization.

Declaration of Generative AI and AI-assisted technologies in the writing process

During the preparation of this work, the authors used GPT-4 in order to improve the language. After using this tool/service, the authors reviewed and edited the content as needed and take full responsibility for the content of the publication.

Declaration of competing interest

The authors declare that they have no known competing financial interests or personal relationships that could have appeared to influence the work reported in this paper.

Acknowledgments

The authors gratefully acknowledge the substantial support from Jiangsu Province Science and Technology Department (Project No. BZ2021057) and from the Research Grants Council of the Hong Kong Special Administrative Region, China (Project No. C6003-22Y).

Appendix

Grid convergence test

The entire computational domain is discretized using unstructured tetrahedral and prismatic grids, with boundary layers incorporated at the air–water interface. To minimize numerical errors caused by mesh size, a grid independence study is conducted. Six sets of mesh grids are generated, containing 120, 240, 350, 460, 550, and 680 thousand elements, respectively. Using the test conditions outlined in Table A.1, the time-varying evaporation rates are plotted in Fig. A1. As shown, coarser meshes tend to overestimate the evaporation rate, while further grid refinement beyond 460 thousand elements results in negligible changes to the solution. However, the computational time increases linearly and then exponentially once the number of elements exceeds 460 thousand. Balancing accuracy and computational efficiency, a fine mesh with approximately 460 thousand elements is selected for all calculations in this study. Detailed mesh information is provided in Table A.1.

Furthermore, due to the implementation of a wet surface boundary condition, the transient simulation of moisture transport is highly sensitive to the settings of the time-dependent solver, which can be adjusted by varying the time step size. To balance accuracy and computational efficiency, three different time step sizes (1 min, 5 min, and 10 min) are tested, with the results presented in Fig. A2. As shown, a smaller time step size, such as 1 min, captures more detailed variations in moisture transport; however, this comes at the cost of significantly increased computational time. When the time step size is increased to 5 min, the simulation closely follows the trend established by the 1-min time step, maintaining acceptable accuracy. In contrast, a time step size of 10 min introduces several large discrepancies, deviating noticeably from the 1-min reference. In conclusion, a time step size of 5 min is selected for this study, as it effectively balances the need for accuracy with the constraints of computational resources.

Validation of the numerical results

To verify the validity of the proposed numerical model, the results are validated against three different types of experimental results: the laboratory-scale model validation, the medium-sized pool validation, and the outdoor large-sized pool validation. The experimental data were summarized by [50].

Test A: Validation of a laboratory-scale model

In the experimental tests conducted by Asdrubali [49], a scale model of a swimming pool was tested under steady-state conditions within a chamber measuring 700 mm × 660 mm × 680 mm. An aluminum container filled with water was placed in the lower section (250 mm × 150 mm × 70 mm) and insulated with polyurethane to ensure that heat transfer occurred exclusively at the air–water interface. Additionally, the air velocity above the interface was set at 0.05 m/s and 0.17 m/s, with measurements taken from five different positions at a height of 10 mm above the water surface. The ambient temperature ranged from 22 °C to 32 °C, and the water temperature was consistently maintained at two degrees lower than the air temperature. The relative humidity varied from 50% to 70%. Several typical cases were numerically tested, specifically with a wind velocity of 0.17 m/s, a relative humidity of 60%, and water temperatures ranging from 20 to 30 °C in increments of 1 °C.

As illustrated in Fig. A3, the multiphysics model developed generally captures the trend of water evaporation as the water temperature

Table A.1
Summary of initial conditions and selected meshing details.

Test conditions		Meshing details	
Air temperature (T_a)	25 °C	No. of elements	464 227
Water temperature (T_w)	20 °C	Average element quality	0.72
Relative humidity (RH)	50%	No. of layer inflation	10
Wind speed	1 m/s	First layer thickness	0.00035 m
Heat input	884 W/m^2	Growth ratio	1.2
Heat input position	Bottom	Average y$^+$ value for air flow	≈1.3
Calculation time	1 h	Average y$^+$ value for water flow	≈32

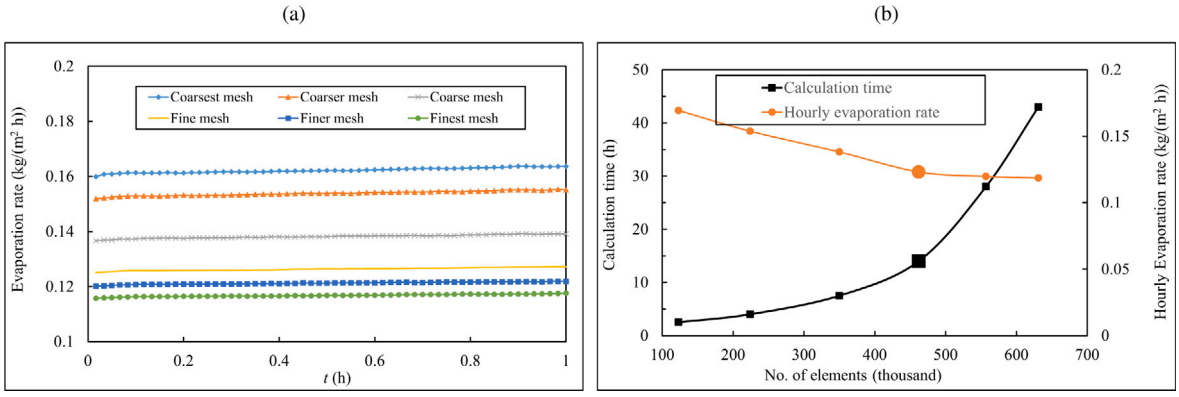

Fig. A1. Grid convergence test (a) time-varying evaporation rate in an hour and (b) evaporation rate and calculation time with respect to number of elements.

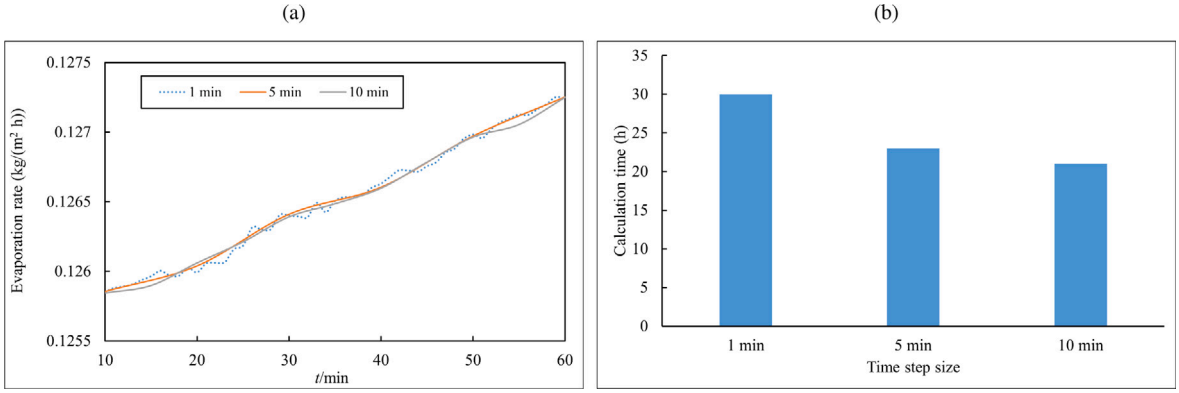

Fig. A2. Time step size selection (a) time-varying evaporation rate with different time step sizes and (b) calculation time at different time step sizes.

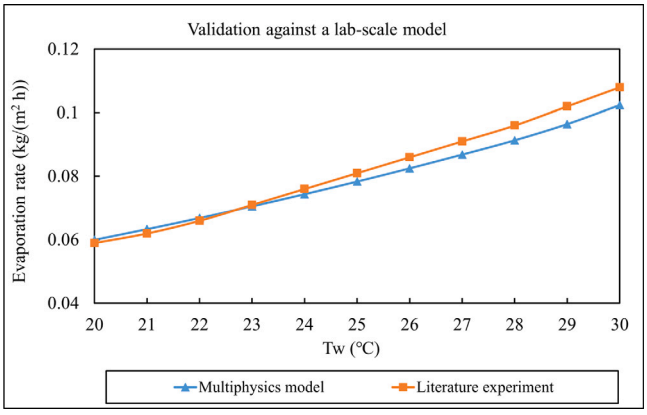

Fig. A3. Validation between experimental results [49] and the multiphysics model for scale model at RH = 60%, V = 0.17 m/s and T_a = 22~32 °C.

increases. However, some discrepancies are noted. Specifically, when the water temperature is below 23 °C, the numerical model tends to overestimate the water evaporation rate, while when temperatures are above 23 °C, it tends to underestimate the evaporation rate. In particular, the maximum deviation between the numerical model and the experimental results occurs at 30 °C, with a relative difference of 5%.

To further assess the validity of our numerical model for small-sized pools, we compared it with another experiment conducted by Blázquez et al. [51]. The experiments were performed in a square-section aluminum wind tunnel measuring 30 cm × 30 cm, with a total length of 1 m. The water container was positioned 65 cm from the inlet of the wind tunnel and had dimensions of 32.5 cm × 32.5 cm × 3.5 cm. External forced convection was provided by a fan located at the beginning of the tunnel with a variable speed drive. The air temperature was controlled by a battery of electrical resistances, while the water temperature was maintained at a constant value using an additional electrical resistance.

Table A.2 presents nine different experimental tests reported in the literature, with airflow velocities ranging from 0.08 m/s to 0.55 m/s

Table A.2
Summary of testing conditions by Blázquez et al. [51].

Wind velocity (m/s)	Air temperature (°C)	Water temperature (°C)	Relative humidity (%)
0.55	26.1	23.9	47.3
0.55	28.1	26.1	68.4
0.55	30.3	28	33
0.24	27.3	25.2	69
0.24	28.1	26.2	63
0.24	30.2	27.7	47
0.08	26	24.2	49.5
0.08	28.5	26	59.3
0.08	30.1	27.8	54.5

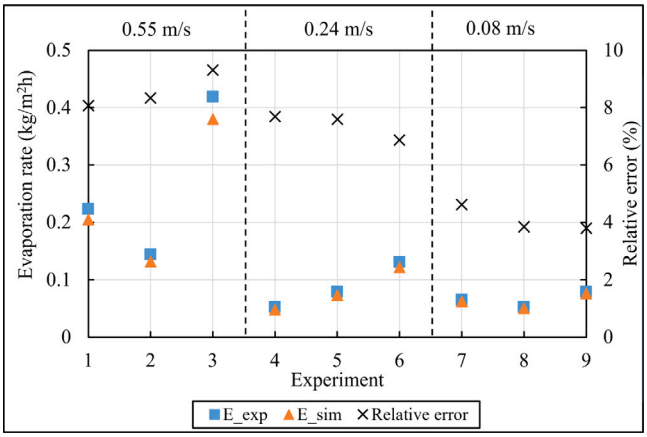

Fig. A4. Validation between experimental results [51] and the multiphysics model under 9 different experimental conditions.

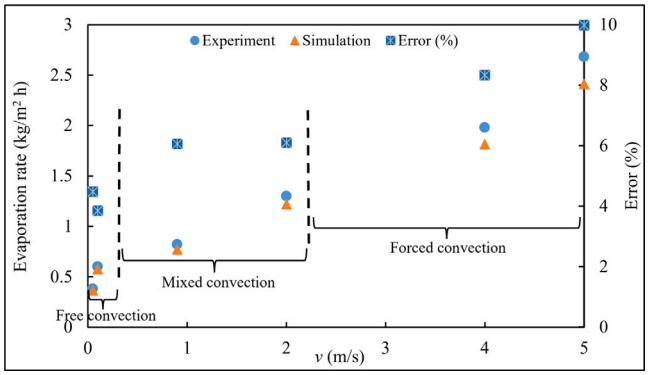

Fig. A5. Validation between experimental results [52] and the multiphysics model at V = 0.05 m/s, 0.1 m/s, 0.9 m/s, 2 m/s, 4 m/s and 5 m/s, T_a = 25 °C and T_w = 35 °C.

and relative humidity values between 33% and 69%. The comparison of results between the experiments and simulations is illustrated in Fig. A4. Overall, the simulation results align well with the experimental data, exhibiting an acceptable relative error of less than 9%. However, the simulation consistently underestimated the experimental results across all conditions, with the relative error varying from 4% to 8.5% as the airflow velocity increased from 0.08 m/s to 0.55 m/s. This discrepancy is arisen because the location of the wind speed measurement in the experimental setup, where the anemometer was positioned behind the pool at a greater distance from the fan, affects the recorded values. The influence of viscous forces near the ground results in the actual inlet wind speed being higher than the measured value, leading to a higher evaporation rate than modeled.

Test B: Validation of medium-sized pools

The numerical solutions have been further validated against the medium-sized pools investigated by Jodat et al. [52], which experimentally examined the effects of surface gravity waves on water evaporation rates across various airflow regimes. The experimental setup consisted of a wave flume integrated with a wind tunnel. The main flume measures 10 m in length, 0.5 m in width, and 0.6 m in height, with a water depth of 0.35 m. The wind tunnel, designed to facilitate airflow over the water surface, is 2 m long, 0.5 m wide, and 0.8 m high. The evaporation rates at steady state, obtained under three distinct airflow regimes without accounting for surface gravity waves, were utilized for comparison with the multiphysics model. During the experiments, the air temperature was maintained at 25 °C, while the water temperature was set at 35 °C. Wind velocities varied from 0.05 m/s to 5 m/s, with increments of 0.1 m/s, 0.9 m/s, 2 m/s, and 4 m/s.

The comparison between the experimental data and the multiphysics model is illustrated in Fig. A5. Overall, the numerical model aligns closely with the experimental results. Notably, the relative error increases from the free convection regime to the mixed convection regime, and further into the forced convection regime, with a maximum relative error of around 10% observed in the forced convection regime. This discrepancy may be attributed to our assumption that neglects the formation of ripples on the water surface under windy conditions, which have been shown to enhance water evaporation [52]. As wind speed increases from 0.05 m/s to 5 m/s, the intensity of surface ripples also rises, leading to a corresponding increase in the predictive error between the multiphysics model and the experimental observations.

Additionally, the multiphysics model is validated against the experiment conducted by Hyldgård [53], in which the evaporation rate was measured under various conditions at steady state. A platform, elevated to a height of 0.2 m, featuring a 7 m^2 basin with a depth of 0.18 m, was located in a room with dimensions of 5.43 m × 3.6 m × 2.42 m (length × width × height). The experimental conditions used for validation are summarized in Table A.3, which include a wind velocity of 0.15 m/s, air temperatures ranging from 24 to 34 °C, water temperatures of 24 and 28 °C, and relative humidity levels of 40, 50, and 70%.

The comparison between the experimental results and the multiphysics model results is illustrated in Fig. A6. Among the 20 different experimental conditions at steady state, the multiphysics model generally aligns with the experimental results, exhibiting a minimum difference of 2% and a maximum difference of 8.75%. Under conditions with lower evaporation rates, the predicted errors are relatively small; conversely, these errors increase with enhanced evaporation conditions. In general, the predicted values fall consistently below the experimental results, similar to the findings of scale model validation.

The primary factor contributing to the observed discrepancies between the experimental and numerical results for both Test A and Test B, particularly under conditions of intense evaporation, is the neglect of Stefan flow in the used evaporation model, as illustrated in Fig. 3. Stefan flow plays a crucial role in the transport of water vapor away from the wet surface. By not considering this flow, the model may underestimate the actual mass transfer that occurs during the evaporation process, leading to inaccuracies in the predicted evaporation rates.

In contrast, the open boundary condition employed in the simulation assumes an unlimited volume of air available to absorb moisture

Table A.3
Summary of testing conditions.

Wind velocity (m/s)	Air temperature (°C)	Water temperature (°C)	Relative humidity (%)
0.15	24	24	40
0.15	25	24	40
0.15	26	24	40
0.15	27	24	40
0.15	28	24	40
0.15	29	24	40
0.15	30	24	40
0.15	24	24	70
0.15	25	24	70
0.15	26	24	70
0.15	27	24	70
0.15	28	24	70
0.15	29	24	70
0.15	28	28	50
0.15	29	28	50
0.15	30	28	50
0.15	31	28	50
0.15	32	28	50
0.15	33	28	50
0.15	34	28	50

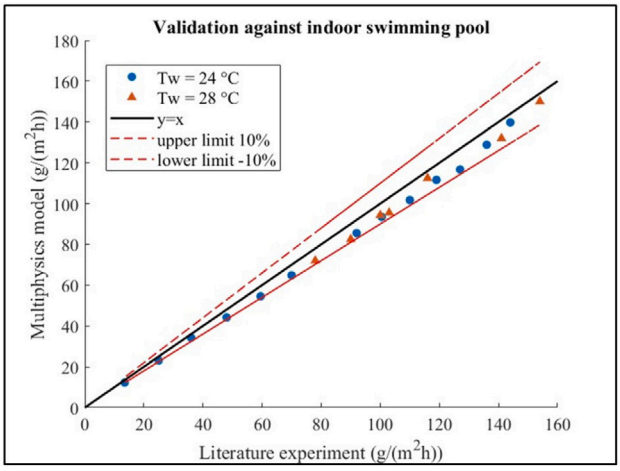

Fig. A6. Validation between experimental results [53] and the multiphysics model for indoor swimming pool at RH = 40%, 50% and 60%, V = 0.15 m/s, T_a = 24~34 °C and T_w = 24 and 28 °C.

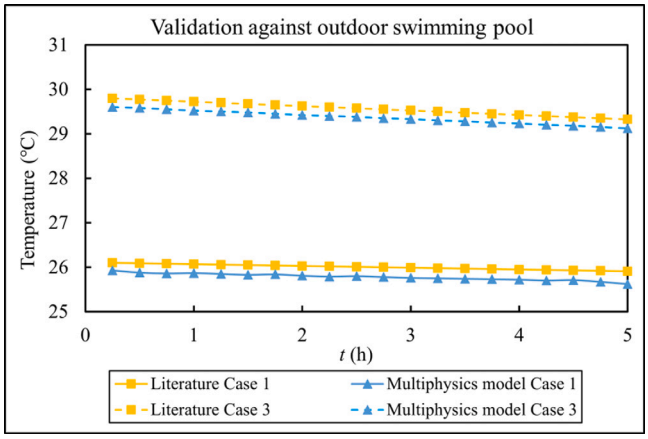

Fig. A7. Validation between experimental results [54] and the multiphysics model for outdoor swimming pool, Case 1: T_a = 19.65 °C, RH = 82.64%, V = 0.9 m/s, and Case 3: T_a = 21.59 °C, RH = 66.41%, V = 1.49 m/s.

from the water surface. This assumption fails to adequately capture the gradual buildup of humidity above the water surface, which is characteristic of an enclosed indoor environment. Consequently, this leads to an underestimation of the evaporation rate in the simulation, particularly at higher water temperatures, where the disparity in vapor pressures, and thus the driving force for evaporation, is more pronounced.

Test C: Validation of outdoor large-sized pools

After being validated in two types of semi-confined environments, the multiphysics model is further verified against an outdoor swimming pool tested by Bernhard et al. [54] to assess its validity in an open environment. In the experimental test, a full-size swimming pool with dimensions of 25 m × 25 m × 2.3 m (length × width × height) was evaluated over time under various conditions. From this, two typical cases were selected for the validation of the multiphysics model: Case 1 with T_a = 19.65 °C, RH = 82.64%, and V = 0.9 m/s; and Case 3 with T_a = 21.59 °C, RH = 66.41%, and V = 1.49 m/s.

The comparison of results is presented in Fig. A7. As observed, the general trends for both cases are consistent within an acceptable difference of less than 4%. The predicted results from the multiphysics model are lower, primarily because of the measurement of wind velocity. Since wind is a vector, the averaged wind velocity in reality may have different directions, which contrasts with the conditions prescribed in the simulation. In the simulation, the direction of the wind is always defined to maximize the effects of the wind on evaporation. Consequently, the water temperature changes more significantly than observed in the literature, indicating that enhanced evaporation is predicted by the multiphysics model.

In general, the established multiphysics model demonstrates a strong capability in accurately estimating water evaporation for the scale model, indoor swimming pool, and outdoor swimming pool. Despite the observed discrepancies, the model performance warrants confidence for the investigations and discussions in this study.

Test D: Validation of roll patterns for Rayleigh–Bénard convection

The roll pattern, a defining feature of Rayleigh–Bénard convection, emerges in fluid as thermally driven circulatory structures during convective processes. These patterns govern the efficiency of vertical heat transport between the lower and upper boundaries, thereby directly modulating the evaporation rates at the water surface. Consequently, accurately resolving the internal convective dynamics within the fluid is essential for robust simulations of evaporative phenomena and constitutes a critical benchmark for evaluating the predictive reliability of the model.

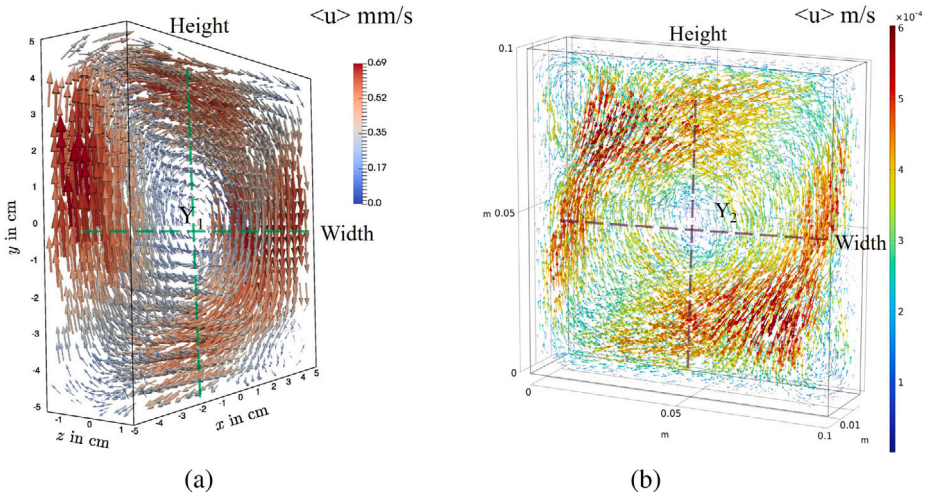

Fig. A8. Validation at 0.25 °C temperature difference, (a) experimental mean velocity field, (b) simulated velocity field.

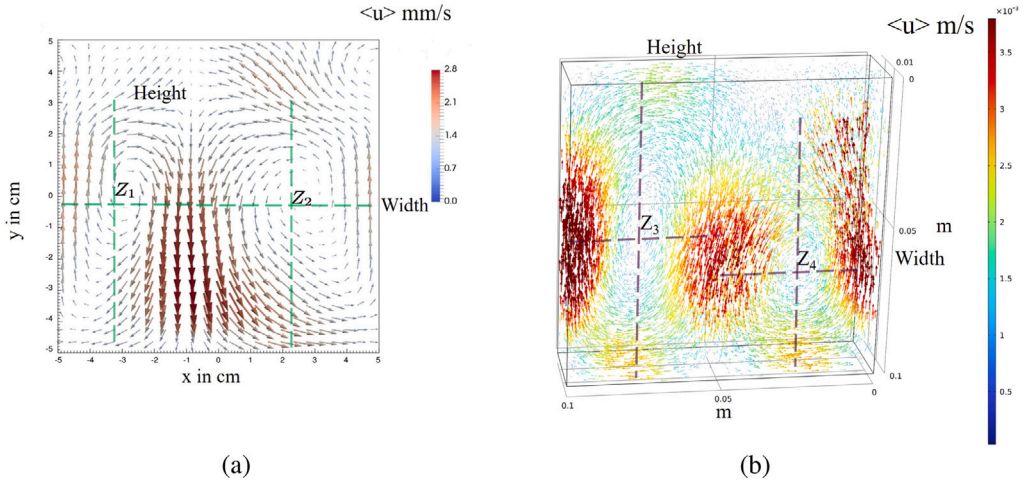

Fig. A9. Validation at 4 °C temperature difference, (a) experimental mean velocity field, (b) simulated velocity field.

Table A.4
Comparison between simulated and experimental roll patterns.

Temperature difference (°C)	Vortex number	Width (cm)	Height (cm)	Maximum flow velocity (mm/s)	Orientation
0.25	Y_1 (experimental)	10	10	0.69	Clockwise
	Y_2 (simulated)	10	8.5	0.61	Clockwise
4	Z_1 (experimental)	4	8	2.8	Clockwise
	Z_2 (experimental)	6	8	2.8	Anticlockwise
	Z_3 (simulated)	5	10	3.5	Clockwise
	Z_4 (simulated)	5	8	3.5	Anticlockwise

Building on the experimental characterization of large-scale flow structures in a rectangular Rayleigh–Bénard sample reported by Horstmann et al. [55], the geometry of the multiphysics model is modified to replicate the experimental setup to simulate natural convection within the system. The dimensions of the aqueous domain are 10 cm × 2.5 cm × 10 cm (length × width × height). Adiabatic boundary conditions are applied to all side surfaces of the model to simulate the auxiliary thermal insulation devices that surround the container in the experimental system. The upper and lower surfaces are set to fixed temperatures to maintain vertical temperature gradients of ΔT = 0.25 °C and 4 °C, which is consistent with the experimental scenarios corresponding to the cases of laminar and turbulent flow, respectively.

The comparison results are presented in Figs. A8 and A9. It is observed that the numerical model can effectively capture both the flow pattern and velocity magnitude within the water body when there is a small temperature difference between the upper and lower surfaces. As the thermal gradient increases, the internal convective flow undergoes a transition from the laminar to the turbulent regime. At a temperature differential of 4 °C, the flow evolves from a single roll structure to a symmetric bifurcated state characterized by two primary counter-rotating vortices of nearly equal magnitude.

To rigorously validate the model's ability to accurately represent natural convection roll patterns, quantitative comparisons between simulated and experimental flow structures under the two temperature difference conditions are conducted across three dimensions: size, flow velocity, and orientation.

Although the numerical simulation successfully captured the fundamental flow structure, the turbulence model exhibited restrictions

in resolving transitional characteristics within sensitive flow regimes. The comparative analysis with experimental measurements reveals two critical modeling limitations: (1) inadequate capture of small-scale vortices, and (2) overestimation of flow velocity induced by errors in wall functions when computing near-wall flow characteristics. However, the temperature differences in the water induced by solar heating are sufficient to ensure that convection within the water remains turbulent in this study, thus significantly mitigating modeling uncertainties and yielding reliable results.

Data availability

Data will be made available on request.

References

[1] K. Xiao, T.J. Griffis, J.M. Baker, P.V. Bolstad, M.D. Erickson, X. Lee, J.D. Wood, C. Hu, J.L. Nieber, Evaporation from a temperate closed-basin lake and its impact on present, past, and future water level, J. Hydrol. 561 (2018) 59–75.

[2] X. Luo, X. Gu, J. Shi, C. Zhao, H. Bao, Thermal design strategy for enhanced freshwater harvesting with interfacial evaporation, Appl. Therm. Eng. 216 (2022) 119104.

[3] P. Mazzei, F. Minichiello, D. Palma, HVAC dehumidification systems for thermal comfort: a critical review, Appl. Therm. Eng. 25 (5–6) (2005) 677–707.

[4] P.M. Cuce, S. Riffat, A state of the art review of evaporative cooling systems for building applications, Renew. Sustain. Energy Rev. 54 (2016) 1240–1249.

[5] H. Chen, J.J. Huang, H. Li, Y. Wei, X. Zhu, Revealing the response of urban heat island effect to water body evaporation from main urban and suburb areas, J. Hydrol. 623 (2023) 129687.

[6] D. Mazzeo, N. Matera, G. Peri, G. Scaccianoce, Forecasting green roofs' potential in improving building thermal performance and mitigating urban heat island in the mediterranean area: An artificial intelligence-based approach, Appl. Therm. Eng. 222 (2023) 119879.

[7] H.L. Penman, Natural evaporation from open water, bare soil and grass, Proc. R. Soc. Lond. Ser. A Math. Phys. Sci. 193 (1032) (1948) 120–145.

[8] W.-K. Song, Y. Chen, Modelling of evaporation from free water surface, Geomech. Eng. 21 (3) (2020) 237.

[9] S. Han, F. Guo, Evaporation from six water bodies of various sizes in east Asia: An analysis on size dependency, Water Resour. Res. 59 (6) (2023) e2022WR032650.

[10] A.M. Raimundo, A.R. Gaspar, A.V.M. Oliveira, D.A. Quintela, Wind tunnel measurements and numerical simulations of water evaporation in forced convection airflow, Int. J. Therm. Sci. 86 (2014) 28–40.

[11] T. Poós, E. Varju, Mass transfer coefficient for water evaporation by theoretical and empirical correlations, Int. J. Heat Mass Transfer 153 (2020) 119500.

[12] K. Heck, E. Coltman, J. Schneider, R. Helmig, Influence of radiation on evaporation rates: A numerical analysis, Water Resour. Res. 56 (10) (2020) e2020WR027332.

[13] S. Bower, J. Saylor, A study of the Sherwood–Rayleigh relation for water undergoing natural convection-driven evaporation, Int. J. Heat Mass Transfer 52 (13–14) (2009) 3055–3063.

[14] N. Kumar, J.H. Arakeri, Natural convection driven evaporation from a water surface, Procedia IUTAM 15 (2015) 108–115.

[15] S. Misyura, R. Egorov, V. Morozov, A. Zaitsev, Evaporation of a water layer under local non-isothermal heating, Appl. Therm. Eng. 219 (2023) 119383.

[16] S.M. Aldarabseh, Evaporation Rate from Free Water Surface, Western Michigan University, 2020.

[17] M. Inan, Ş. ÖZGÜR ATAYILMAZ, Experimental investigation of evaporation from a horizontal free water surface, Sigma: J. Eng. Nat. Sci./ Mühendislik Bilim. Derg. 35 (1) (2017).

[18] A. Jodat, M. Moghiman, M. Anbarsooz, Experimental comparison of the ability of dalton based and similarity theory correlations to predict water evaporation rate in different convection regimes, Heat Mass Transf. 48 (2012) 1397–1406.

[19] C.-R. Chu, M.-H. Li, Y.-Y. Chen, Y.-H. Kuo, A wind tunnel experiment on the evaporation rate of class a evaporation pan, J. Hydrol. 381 (3–4) (2010) 221–224.

[20] J.R. Masoner, D.I. Stannard, A comparison of methods for estimating open-water evaporation in small wetlands, Wetlands 30 (3) (2010) 513–524.

[21] G.P. Rodrigues, Í.S. Rodrigues, A. Raabe, P. Holstein, J.C. de Araújo, Direct measurement of open-water evaporation: a newly developed sensor applied to a Brazilian tropical reservoir, Hydrol. Sci. J. 68 (3) (2023) 379–394.

[22] M.E. Jensen, Estimating evaporation from water surfaces, in: CSU/ARS Evapotranspiration Workshop, Fort Collins, CO, 2010, pp. 1–27.

[23] F.E. Jones, Evaporation of Water with Emphasis on Applications and Measurements, CRC Press, 2018.

[24] M. Al-Shammiri, Evaporation rate as a function of water salinity, Desalination 150 (2) (2002) 189–203.

[25] K. Friedrich, R.L. Grossman, J. Huntington, P.D. Blanken, J. Lenters, K.D. Holman, D. Gochis, B. Livneh, J. Prairie, E. Skeie, et al., Reservoir evaporation in the western United States: current science, challenges, and future needs, Bull. Am. Meteorol. Soc. 99 (1) (2018) 167–187.

[26] M.T. Pauken, S. Jeter, S. Abdel-Khalik, B. Farley, An Experimental Investigation of Water Evaporation into Low-Velocity Air Currents, Technical Report, American Society of Heating, Refrigerating and Air-Conditioning Engineers ..., 1995.

[27] F.P. Incropera, D.P. DeWitt, T.L. Bergman, A.S. Lavine, et al., Fundamentals of Heat and Mass Transfer, Vol. 6, Wiley New York, 1996.

[28] M. Muneeshwaran, H.-Y. Lin, C.-M. Yang, K. Nawaz, C.-C. Wang, Universal correlation for falling film evaporation heat transfer coefficients of water and seawater, Appl. Therm. Eng. 259 (2025) 124881.

[29] K. Hisatake, M. Fukuda, J. Kimura, M. Maeda, Y. Fukuda, Experimental and theoretical study of evaporation of water in a vessel, J. Appl. Phys. 77 (12) (1995) 6664–6674.

[30] D. Wickert, G. Prokop, Simulation of water evaporation under natural conditions—A state-of-the-art overview, Exp. Comput. Multiph. Flow 3 (2021) 242–249.

[31] J.L.F. Blázquez, I.R. Maestre, F.J.G. Gallero, P.Á. Gómez, A new practical CFD-based methodology to calculate the evaporation rate in indoor swimming pools, Energy Build. 149 (2017) 133–141.

[32] F.J.G. Gallero, I.R. Maestre, J.L. Foncubierta Blazquez, J.D. Mena Baladés, Enhanced CFD-based approach to calculate the evaporation rate in swimming pools, Sci. Technol. Built Environ. 27 (4) (2020) 524–532.

[33] P. Ciuman, B. Lipska, Experimental validation of the numerical model of air, heat and moisture flow in an indoor swimming pool, Build. Environ. 145 (2018) 1–13.

[34] D. Lovell, T. Rickerby, B. Vandereydt, L. Do, X. Wang, K. Srinivasan, H. Chua, Thermal performance prediction of outdoor swimming pools, Build. Environ. 160 (2019) 106167.

[35] W. Zimmerman, Introduction to COMSOL multiphysics, in: Multiphysics Modeling with Finite Element Methods, World Scientific, 2006, pp. 1–26.

[36] T.R. Oke, Boundary Layer Climates, Routledge, 2002.

[37] A. RG, Crop evapotranspiration: guidelines for computing crop water requirements, FAO Irrig Drain 56 (1998) 147–151.

[38] A. Ferrari, A. Kubilay, D. Derome, J. Carmeliet, Design of smart wetting of building materials as evaporative cooling measure for improving the urban climate during heat waves, in: 12th Nordic Symposium on Building Physics, NSB 2020, Vol. 172, EDP Sciences, 2020, p. 3001.

[39] W. Heitz, J. Westwater, Critical Rayleigh numbers for natural convection of water confined in square cells with L/D from 0.5 to 8, J. Heat Transf. (1971).

[40] H. Kasedde, A. Namagambe, J.D. Lwanyaga, J.B. Kirabira, D. Okumu, Numerical modelling of a solar salt pan for improved salt production at Lake Katwe, Uganda, Case Stud. Therm. Eng. 42 (2023) 102592.

[41] C. Hrenya, E. Bolio, D. Chakrabarti, J. Sinclair, Comparison of low Reynolds number k- ε turbulence models in predicting fully developed pipe flow, Chem. Eng. Sci. 50 (12) (1995) 1923–1941.

[42] Y. Menni, H. Ahmad, H. Ameur, S. Askar, T. Botmart, M. Bayram, G. Lorenzini, Effects of two-equation turbulence models on the convective instability in finned channel heat exchangers, Case Stud. Therm. Eng. 31 (2022) 101824.

[43] N. Deng, P. Dong, Z. Wang, M. Li, Quantifying the effects of spectral and directional distribution of radiation on its propagation in saline water, Appl. Therm. Eng. 258 (2025) 124536.

[44] A. Koca, H.F. Oztop, Y. Varol, The effects of Prandtl number on natural convection in triangular enclosures with localized heating from below, Int. Commun. Heat Mass Transfer 34 (4) (2007) 511–519.

[45] S. Khandekar, K. Muralidhar, M. Bhendura, K. Muralidhar, S. Khandekar, Introduction to evaporative heat transfer, in: Drop Dynamics and Dropwise Condensation on Textured Surfaces, Springer, 2020, pp. 131–146.

[46] Y. Chen, W. Hu, J. Wang, F. Hong, P. Cheng, Transient effects and mass convection in sessile droplet evaporation: The role of liquid and substrate thermophysical properties, Int. J. Heat Mass Transfer 108 (2017) 2072–2087.

[47] M. Bhendura, K. Muralidhar, S. Khandekar, Determination of evaporation rate of warm water placed inside a partially-filled top cooled enclosure, Int. J. Therm. Sci. 179 (2022) 107612.

[48] G. Niedrist, R. Psenner, R. Sommaruga, Climate warming increases vertical and seasonal water temperature differences and inter-annual variability in a mountain lake, Clim. Change 151 (2018) 473–490.

[49] F. Asdrubali, A scale model to evaluate water evaporation from indoor swimming pools, Energy Build. 41 (3) (2009) 311–319.

[50] M.M. Shah, Further development and verification of the model for evaporation from pools, Sci. Technol. Built Environ. 29 (1) (2023) 75–85.

[51] J.L.F. Blázquez, I.R. Maestre, F.J.G. Gallero, P.Á. Gómez, Experimental test for the estimation of the evaporation rate in indoor swimming pools: Validation of a new CFD-based simulation methodology, Build. Environ. 138 (2018) 293–299.

[52] A. Jodat, M. Moghiman, G. Shirkhani, An experimental investigation on the effects of surface gravity waves on the water evaporation rate in different air flow regimes, Heat Mass Transf. 49 (2013) 1823–1830.

[53] C.-E. Hyldgård, Water Evaporation in Swimming Baths, Institut for Bygningsteknik, Aalborg Universitet, 1990.
[54] M. Bernhard, O. Marc, E. Quilichini, J. Castaing-Lasvignottes, Sensitivity analysis of an outdoor swimming pool under dynamic conditions, Procedia Manuf. 35 (2019) 124–129.
[55] G.M. Horstmann, D. Schiepel, C. Wagner, Experimental study of the global flow-state transformation in a rectangular Rayleigh–Bénard sample, Int. J. Heat Mass Transfer 126 (2018) 1333–1346.